uOttawa

Experimental and Computational Investigations of Halogen-Bonded Systems and their NMR Parameters

Dan Zheng

A thesis submitted in partial fulfilment of the requirements for the MSc degree in Chemistry

Department of Chemistry and Biomolecular Sciences

Faculty of Science

University of Ottawa

Table of Contents

List of Figures

List of Tables

Acknowledgement

If I see the day to have my Masters' thesis submitted and reviewed, then I know I owe it to quite a lot of people and resources. In my case, these people are certainly composed of the dear Bryce Group, as everyone supported each other during the pandemic times both on the academic and personal levels.

Thank you infinitely Dr. Bryce for letting me pursue this Masters' degree in your group, thank you for all the zoom check-ins and virtual help during the pandemic learning times and all the in-person counselling when we were back in the lab! Thank you for sharing your knowledge with the whole team and for being supportive. I also want to show gratitude and many thanks to Dr. Patrick Szell for all his support and big help for pushing our project forward and showing me all the different facets of paper writing along with (quite advanced and sometimes too complex for me I must say) detailed NMR experiments and introducing me to the joys of NQR. That part of my project would not have been completed if Pat was not there and I wouldn't have learned half as much if it weren't for all his project insights, explanations, tips and also general life wisdom and anecdotes. I am very grateful for all your help and encouragement Pat, thank you sincerely.

I also want to thank Professor Giorgi and Professor St-Amant for being my thesis committee members and for kindly reviewing my thesis.

To my friends from the Bryce lab, thank you all for your kindness, smiles (behind your masks), help and support. I would not have been able to complete all the NMR experiments without the help of Tamali Nag, PhD student in our group, and Vincent Morin, our NMR technician as well as an old member of the Bryce Lab and a dear friend of mine. I

wish all of our team the best of success in the future. It was also an honour for me as a graduate student to have been the mentor and supervisor of Mahée Côté, a very hard-working summer student in the Bryce Group and now a close friend of mine. Mahée, I wish you all the best for the future and I know you will be accomplishing wonders after your studies!

Finally, I would like to show my gratitude to Dr. Peter Pallister and Dr. Jeffrey Ovens for all their help and assistance in my NMR and PXRD trainings and experiments, and also for their time answering any technical questions and general inquiries.

Abstract

Halogen bonding to phosphorus atoms remains uncommon, with relatively few examples reported in the literature. In part 1 of the thesis, the preparation and investigation of the cocrystal (dicyclohexylphenylphosphine)(1,6-diiodoperfluorohexane) by X-ray crystallography and solid-state multinuclear magnetic resonance spectroscopy is described. The crystal structure features two crystallographically unique C-I···P halogen bonds ($d_{I\cdots P}$ = 3.090(5) Å, 3.264(5) Å) and crystallographic disorder of one of the 1,6-diiodoperfluorohexane molecules. The first of these is the shortest and most linear I···P halogen bond reported to date. ^{13}C, ^{19}F, and ^{31}P magic-angle spinning solid-state NMR spectra are reported. A ^{31}P chemical shift change of -7.0 ppm in the cocrystal relative to pure dicyclohexylphenylphosphine, consistent with halogen bond formation, is noted. This work establishes iodoperfluoroalkanes as viable halogen bond donors when paired with phosphorus acceptors, and also shows that dicyclohexylphenylphosphine can act as a practical halogen bond acceptor.

In part 2 of the thesis, computational work was done on nuclides of atoms which engage in the strongest halogen bonds (iodine, bromine, chlorine) that are all quadrupolar (spin $I >$ ½). Previous group work reported extensive experimental NMR and NQR data relating $^{35/37}Cl$, $^{79/81}Br$, and ^{127}I quadrupolar coupling information to local molecular structure in halogen bonded systems. Here, we make use of a new parameter, the valence p-orbital population anisotropy (VPPA), reported by Rinald and Wu, to increase our understanding of the origins of the electric field gradients (EFG) in halogen-bonded systems. Computations on model and real halogen-bonded cocrystalline systems using standard hybrid DFT methods are used to generate p-orbital populations and to compute the VPPA. We discuss the utility of the VPPA,

and hence the EFG, as a tool to assess the ability of particular donors to engage in halogen bonds.

Chapter 1: Introduction

1.1- To bond or not to bond?

What is a bond? What is a chemical bond? Looking at a very simple definition from the Oxford dictionary, a chemical bond is a strong force of attraction holding atoms together in a molecule or crystal, resulting from the sharing or transfer of electrons.[1] From more scientific literature, "chemical bonds hold molecules together and create temporary connections that are essential to life. Types of chemical bonds include covalent, ionic, and hydrogen bonds and London dispersion forces."[2] All living things are made up of atoms, and since these atoms aren't just floating around by themselves, they are interacting with other atoms and together, these form all matter around us. When speaking of chemical bonds, we know some can be very strong just like others are quite weak and only form temporarily. Both are important and are essential to the existence of all form of life. But why do atoms want to form bonds with other atoms? The best answer in regards to energy is that atoms want to reach the most stable (lowest energy) state. Atoms may do so when their valence shell of electrons is filled and when they satisfy the octet rule of having 8 valence electrons. They may do so by sharing electrons through bonds and the four major types of chemical bonds are covalent bonds, ionic bonds, hydrogen bonds and Van der Waals interactions, with the last three falling under the category of noncovalent bonds.

Let us start with the covalent bond; this is formed due to the stable balance of attractive and repulsive forces that are present between atoms when they share and exchange electrons. By sharing electrons, this will allow the atoms to have a full outer shell of electrons. Normally, this type of bond is most common between two non-metals having similar electronegativity and between an electron (negatively charged ion) with a metal (positively charged) ion.

Covalent bonds can be separated into two types: polar and nonpolar covalent bonds (see Figure 1). The polar covalent bond exists between two atoms with an electronegativity difference of 0.4 to 1.7 whereas for nonpolar covalent bonds, the electronegativity difference is smaller than 0.4 (there is no polarity).[3] When the electronegativity difference value is high, it means one of the atoms (the one with the higher electronegativity value) attracts the electrons more than the other atom, making the bond polar.

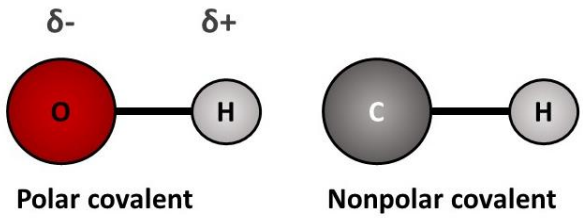

Figure 1: Example of covalent bonds. OH is a polar covalent bond and CH is a nonpolar covalent bond

The bond type we are quite interested in for the purpose of this thesis is the noncovalent bond, as halogen bonds are part of this group. Noncovalent bonds are in general weaker bonds than covalent ones since the latter are formed when two atoms share their electrons with each other whereas noncovalent bonds form either by no exchange whatsoever of electrons or complete exchange of electrons between two atoms.[3] When an atom gains or loses electrons it will form a negative or positive charged particle; this is what we call "ions". When two oppositely charged ions (one positive and one negative) come together an electrostatic interaction forms and this is termed the ionic bond. Again, electronegativity influences the strength of the ionic bond; an atom with high electronegativity will attract the electrons of a low electronegativity atom in order to form an ionic bond (see below).

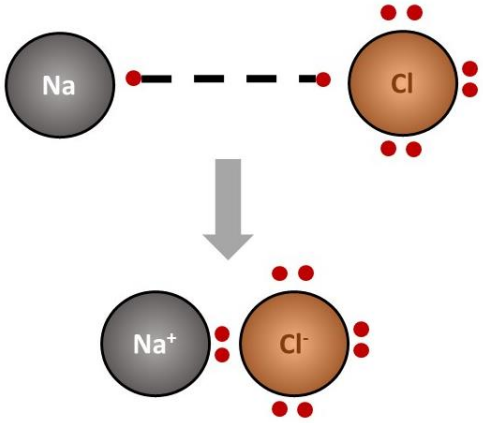

Figure 2: Example of ionic bonding; NaCl forming an ionic bond

Another well-known example of noncovalent bonds is the hydrogen bond, a result of the interaction between a hydrogen atom bonded to an electronegative heteroatom such as oxygen, nitrogen or fluorine, and another lone-pair of electrons on a neighboring nitrogen or oxygen-containing molecule (see Figure 3). Though this intermolecular interaction is considered strong in comparison to certain intramolecular noncovalent interactions (Van der Waals, polar-polar interactions), the typical strength of a hydrogen bond (in the range of 4 to 40 kJ/mol) is about 5% of that of a covalent bond (average of 415 kJ/mol). Please refer to Table 1 for some typical bond energies (values were taken from reference 2).

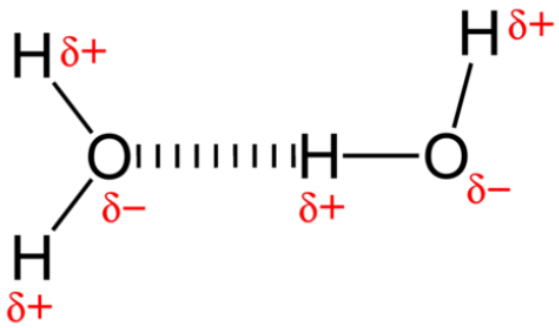

Figure 3: Example of a hydrogen bond in water. The hydrogen atom of one water molecule and the lone pair of electrons on an oxygen atom of a neighbouring water molecule form a hydrogen bond. There is an electrostatic interaction between the partially negative (δ^-) of the oxygen and partially positive (δ^+) of the hydrogen.

Table 1: Typical covalent bond energies

Bond	**Energy (kJ/mol)**	**Bond**	**Energy (kJ/mol)**
H-H	436	I-I	150
H-C	412	C-I	240
H-N	390	C-Cl	330
H-O	464	C = C	611
H-F	569	C = O	741
N = N	418	C ≡ C	837
N ≡ N	946	C ≡ O	1080

A noncovalent bond is also known as a molecular interaction, a non-bonding interaction or an intermolecular forces; they are all synonyms. This brings us to discuss the halogen bond, a type of noncovalent interaction that first gained popularity and started being discussed after the 1950s. Let us recall that the halogen group consists of the following 6 elements: fluorine (F), chlorine (Cl), bromine (Br), iodine (I), astatine (At) and tennessine (Ts).

They are known for their relatively high electronegativity. Halogen atoms can behave as electron-rich (nucleophilic) sites and form net attractive interactions with electron-poor (electrophilic) partners. The term "halogen bond" was only implemented in 1978 by Dumas and coworkers as they studied interactions of CCl_4, CBr_4, $SiCl_4$ and $SiBr_4$ with pyridine, tetrahydropyran, tetrahydrofuran and anisole with different instrumental analysis such as NMR, IR and Raman.[4] It is only until the 1990s that the nature and applications of the halogen bond began to be intensively studied and nowadays there is a growth in range of halogen bonds applications across different sectors of science.[5,6]

1.2- The Halogen Bond

According to IUPAC recommendations, the definition of a halogen bond is a "net attractive interaction between an electrophilic region associated with a halogen atom in a molecular entity and a nucleophilic region in another, or the same, molecular entity"[7]. A visual representation of the halogen bond is provided in Figure 4. There are some indications as to the presence of halogen bonds, and the greater the number of indications satisfied, the higher the probability of halogen bonding. The two most evident features for halogen bonds are geometrical; the first one is that the interatomic distance between the halogen bond donor (X) and halogen bond acceptor (A) must be less than the sum of the van der Waals radii (Equation 1).

$$d_{X\cdots A} \leq \sum d_{\mathrm{vdW}}$$

Equation 1: The distance between the halogen bond donor (X) and halogen bond acceptor (A) must be less than the sum of the van der Waals radii.

The other main feature of a halogen bond is that the D-X···A angle tends to be linear (180°). The halogen bond acceptor A approaches X along the extension of the D-X bond (Equation 2).

$$\theta_{D-X\cdots A} \approx 180°$$

Equation 2: The angle of the halogen bond tends to approach 180°

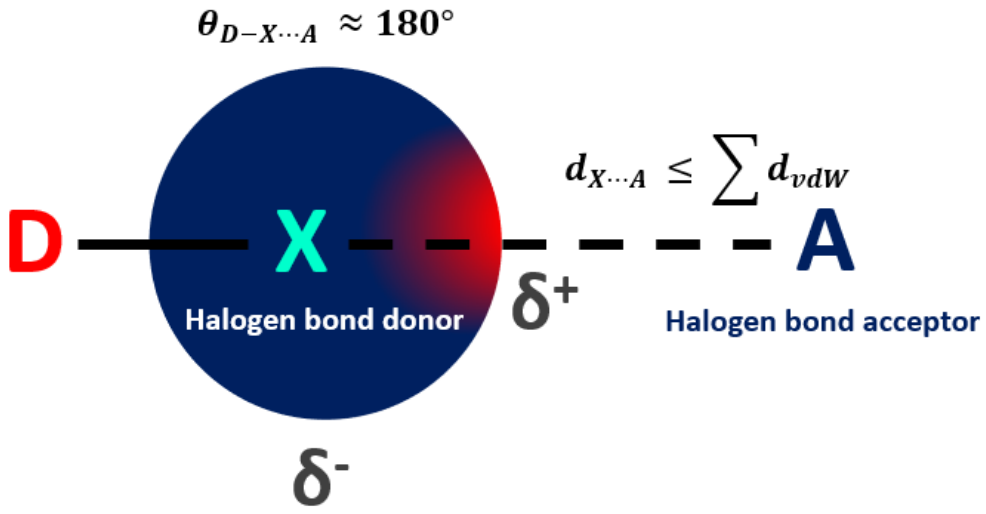

Figure 4: Schematic representation of a halogen bond interaction. X can be F, Cl, Br, I. D represents an electron-withdrawing group. 'A' represents an electron-rich moiety. The partially positive (δ^+) region represents the electrophilic region termed σ-hole.

The halogen has an area of elevated electrostatic potential, called the σ-hole. This σ-hole is due to the anisotropy of the atom and can be explained by the presence of a region of positive electrostatic potential on the outermost portion of the halogen's surface, centered on the D–X axis.[8]

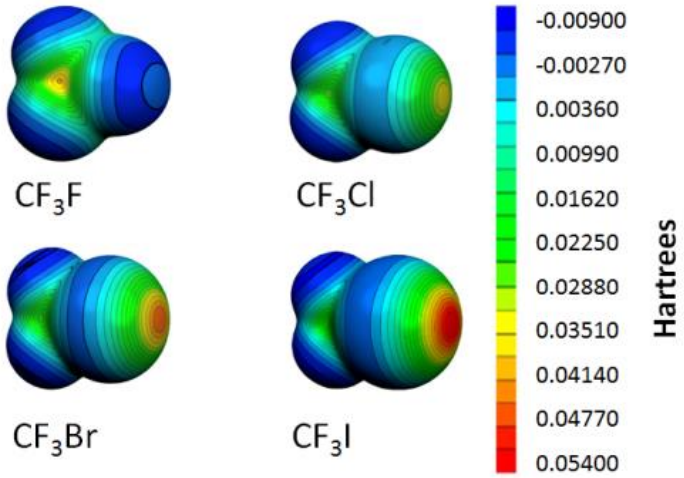

Figure 5: Representation of the σ-hole. The molecular electrostatic potential, in Hartrees, at the 0.001 electrons Bohr^{-3} isodensity surface of CF_3F, CF_3Cl, CF_3Br and CF_3I.[8] This figure was reproduced with permission from the publisher.

The strength of the σ-hole goes down from iodine (strongest σ-hole) to fluorine (weakest σ-hole). Larger halogens will give rise to stronger halogen bonds (I > Br > Cl) and the presence of electron-withdrawing groups enhances the σ-hole. The more electron withdrawing the atom bound to the halogen is, the stronger the halogen bond. The halogen bond energy spans over a wide range, from 5 to 180 kJ/mol. An example of weak halogen bond is the Cl-Cl interaction between chlorocarbons and a very strong halogen interaction is that of $I\text{-}I_2$ in I_3^-.[9] If we are to compare halogen bonding to hydrogen bonding, thanks to its strength, halogen bonding can prevail over hydrogen bonding in selecting the modules to be involved in competitive recognition processes.[10] Halogen bonding is also expected to provide access to molecular assembly motifs involving heavy atoms with increasingly diffuse electron orbitals.[11] Application wise, it has been recently recognized that halogen bonds can play a central role in ligand binding and molecular folding of macromolecules such as proteins and DNA and other various biological processes.[12] Another interesting application is crystal

engineering; co-crystals with specific desired features of structure and composition that can lead to, for example, non-linear optical activity and enhanced conducting properties can be produced.[9]

This master's thesis is composed of two major projects; one is computational and involves using valence p-orbital population anisotropy to further comprehend halogen-bonded systems and quadrupole coupling constants. The second is much more experimental and consists of investigating the quite distinct phosphorus – iodine halogen bond of a new cocrystal by means of solid-state multinuclear magnetic resonance and X-ray crystallography. In this part of the project, we describe an uncommon example of halogen bonding to phosphorus atoms.

Through these two years of research, I was introduced to both DFT and computational methods and experimental NMR and single crystal x-ray diffraction for the analysis of halogen bonds and quadrupolar coupling.

Chapter 2 – Experimental and Theoretical Background

The start of this master's project debuted at the same time as the Covid-19 pandemic. Wet lab projects and studies were therefore laid off for a big part of a semester. To circumvent this obstacle, a first computational project that could be done from home was tackled. The primary goal of this computational study of my master's thesis is to compare how quadrupolar coupling constants vary according to a change in the valence p-orbital population anisotropy (VPPA). To do so, one must first understand the concepts of quadrupolar coupling and nuclear magnetic resonance, commonly known as NMR.

2.1 – Nuclear Magnetic Resonance

Nuclear Magnetic Resonance, commonly referred to as NMR, is one of the most important tools of characterization for all fields of chemistry (organic, inorganic, physical) as it can ease the determination of electronic environments, molecular identity and structures as well as physical, chemical and biological properties of compounds.[13] Simply put, NMR spectroscopy can be considered as a form of absorption spectroscopy where a sample is exposed to a magnetic field and absorbs an electromagnetic radiation in the radiofrequencies (RF) range.[13] Let us recall the definition of spectroscopy as well; it is the study of the interaction between electromagnetic radiation and matter.[14] NMR spectroscopy studies the absorption and interaction of radiofrequency radiation by a nucleus in a magnetic field and the principles are based on the effect of the magnetic field on the net spin of an atom's nucleus. The signal in NMR is produced by absorption of electromagnetic radiation of the appropriate frequency. To get an NMR spectrum, the magnetic field must be varied over a small range and observation of the RF signal from the sample will be translated with peaks of different intensity according to the frequencies.[15]

NMR spectroscopy is continually expanding and finding new applications in protein folding such as determining residual structures of unfolded proteins, molecular dynamics in quantifying motional properties of biomacromolecules, drug screening and design (determining the conformation of enzyme, receptor compounds) and in material science for polymer chemistry and physics.[16]

2.1.1 – Spin

The fundamental basics of NMR are directly related to the magnetic properties of a nucleus. All nuclei contain a charge, and this charge is in rotation along an axis and will generate a magnetic dipole (see Figure 6). The nuclear spin describes the intrinsic angular moment associated with the nucleus, but in reality, the nucleus does not spin.[13]

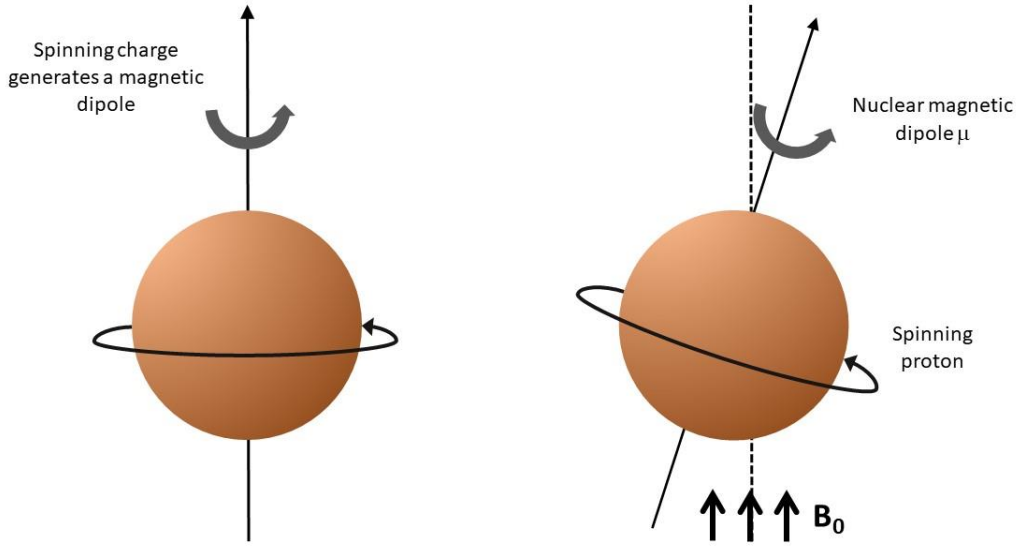

Figure 6: Classical representation of a proton precessing in a magnetic field of magnitude B_0 in analogy with a precessing spinning top.

The symmetry at the atomic scale is examined using the nuclear spin, represented by *I,* of the compound of interest. Quantum mechanics have helped chemists in describing this angular momentum due to the fact that subatomic particles show both of the wave and particle properties (*wave-particle duality*).[17] The angular momentum can have the following values: 0, ½, 1, 1½, etc. (increments of ½) and may be visualized using the classical analogy of the angular momentum of a rotating object.[18] Along with the spinning charge, a magnetic moment m_I having a value of $2I + 1$ is also produced and this is detected by NMR spectroscopy. There is no spin when $I = 0$ since there is no magnetic moment ($2I + 1 = 0$) and therefore no signal will be detected. If $I = 1$, the possible values of m_I may be -1, 0 or 1.[17] When $I = ½$, the spin is an intrinsic property that can be described as "up" or "down" (α and β respectively). This is completely analogous to the case of electrons (also spin-1/2 particles) that are represented as upward and downward arrows in electronic configuration diagrams of atoms (see Figure 7).

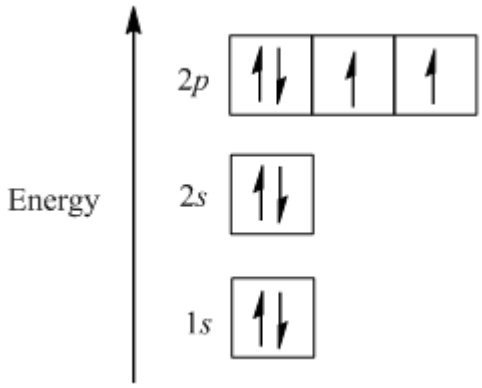

Figure 7: Ground state electronic configuration of oxygen ($1s^2 2s^2 2p^4$). The filling of the molecular orbitals follow the Aufbau principle (filling the lowest energy levels first) and Hund's rule (pairing of electrons takes place only after placing a singly occupied electron into the orbital).

The most common nuclei used in NMR spectroscopy are ^{1}H and ^{13}C, each with an I value of ½. Some other nuclei possessing a spin number of ½ and a spherical and uniform distribution of charge are ^{15}N, ^{19}F and ^{31}P. Now, more than 2/3 of the NMR active nuclei have a spin greater than ½. In the following parts of the theory, the quadrupolar coupling that is exhibited by nuclei with $I > ½$ will be described.

2.1.2 – Zeeman Effect

The Zeeman effect consists of atomic or nuclear level splitting, more specifically the splitting of spectral lines of a sample when it is placed under an external magnetic field. It can be perceived as the separation in the energy levels between the two spin states of a nucleus. Spin states are degenerate in energy, and they can be separated into two different states possessing each an equal amount of energy. If there is an absence of and external applied magnetic field B_0, then the energy of a spin 1/2 nucleus is independent of the orientation of the spin. When a magnetic field is applied, the degeneracy is broken and the energy of the nucleus will depend on the orientation of the spin relative to the applied magnetic field.[17] This spin can either be aligned with the magnetic field ($m_s = -½$) or against the magnetic field ($m_s = +½$). When the magnetic field gets stronger, the energy difference between the two spins will increase linearly as described below.

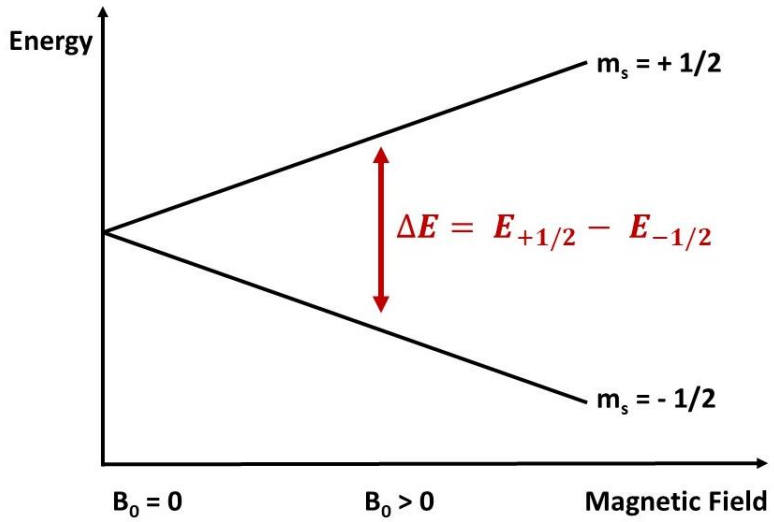

Figure 8: Representation of the Zeeman Effect with increasing magnetic field. The separation in energy will increase linearly as the magnetic field gets stronger.

Figure 8 shows the dependence of ΔE on the strength of the magnetic field. ΔE is the difference in energy between the spin states and it represents the amount of energy needed to send the spins from the lower energy state to the higher energy state.$\Delta E = (h\gamma/2\pi)\, B_0$

Equation 3 indicates the proportional relationship between the energy and the magnetic field.

$$\Delta E = (h\gamma/2\pi)\, B_0$$

Equation 3. Relationship between energy and magnetic field

Where h is the Planck constant, γ is the gyromagnetic ratio and is equal to $2\pi\mu/hI$ (this constant is unique to each nucleus and consists of the proportionality constant between the magnetic moment μ and the spin number I), and B_0 represents the external applied magnetic field.

2.1.2 – Larmor frequency and spin precession

The Larmor frequency (v), another important NMR concept, consists of the particular radiofrequency needed to realize the transition from the lower energy state to a higher one. Named after the mathematical physicist Joseph Larmor from the 19th century, nowadays, in NMR, the Larmor frequency refers to the frequency at which a given nuclear spin precesses in the applied magnetic field. The Larmor frequency equation can be found below, where γ is the gyromagnetic ratio and B_0 is the strength of the magnetic field.[18]

$$v = (\gamma/2\pi)\, B_0$$

Equation 4. Larmor frequency

The gyromagnetic ratio γ is the ratio between the magnetic moment and the angular momentum. It can be determined using the following equation:

$$\gamma = {}^{2\pi\mu}/_{Ih}$$

Equation 5. Gyromagnetic ratio

Spin precession, in turn, is a complex aspect but it can be visualized more simply as a spinning top. When the top rotates initially, its angular momentum is aligned with the Z axis and will deviate from this axis as the top loses speed and slows down. The change in this angular momentum around the Z axis is called precession. In order to achieve this spin precession, a radiofrequency pulse is first applied, then a rotation about the axis occurs, represented by s (spin) in a circular trajectory (see Figure 9 below). Finally, the precession will return to its thermodynamic equilibrium (back towards the **B** field axis).[17]

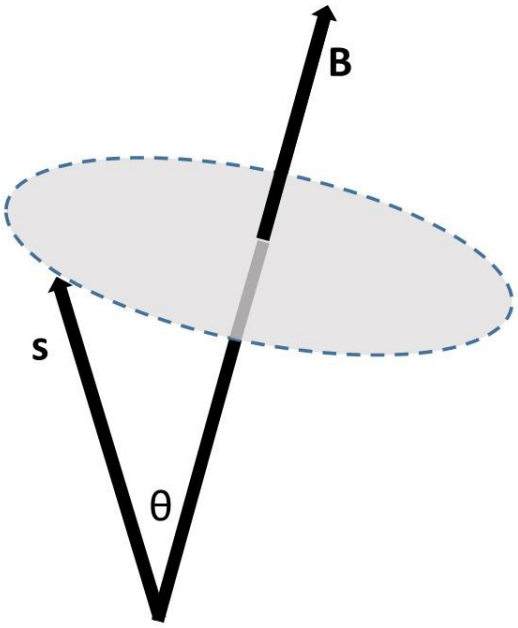

Figure 9: Representation of precessional motion. S traces out the circular motion around B, while keeping θ fixed.

Taking hydrogen (^{1}H) as an example, when a radiofrequency pulse is emitted perpendicular to the magnetic field, a change in the magnetic moment happens and it is projected into the XY plane. The magnetic moments are then detected as they precess back to their thermodynamic equilibrium with the lowest energy state possible.

$$M_y(t) = M_{0,y}\cos(2\pi\nu t)e^{-t/T_2}$$

Equation 6. Position of the magnetization at a time t during the precession

M_0 is the thermodynamic equilibrium, t is the time, T_2 is the spin-spin relaxation time and ν is the Larmor frequency.

To yield all NMR information and to obtain a spectrum, the magnetic moment's precession of a sample is detected and this results in a free induction decay (FID). Then, using Fourier transformation, the NMR frequencies of the nuclei are extracted and an NMR spectrum is produced.

2.2 – Quadrupolar Nuclei

As mentioned previously, the nuclei in the periodic table can be divided into two major parts; those with spin = ½ and the others with spin > ½ (note that certain atoms have more than one isotope and thus both spin equal to ½ and greater than (see Figure 10). There are some with spin 0 as well (even mass nuclei having even numbers of protons and neutrons such as ^{12}C and ^{16}O) Those with spin greater than ½ are called quadrupole nuclei since they possess a nuclear electric quadrupole moment that will interact with the electric-field gradient (EFG) generated by the electrons present in the sample and its surroundings.[18] The EFG will be discussed shortly in the next sections.

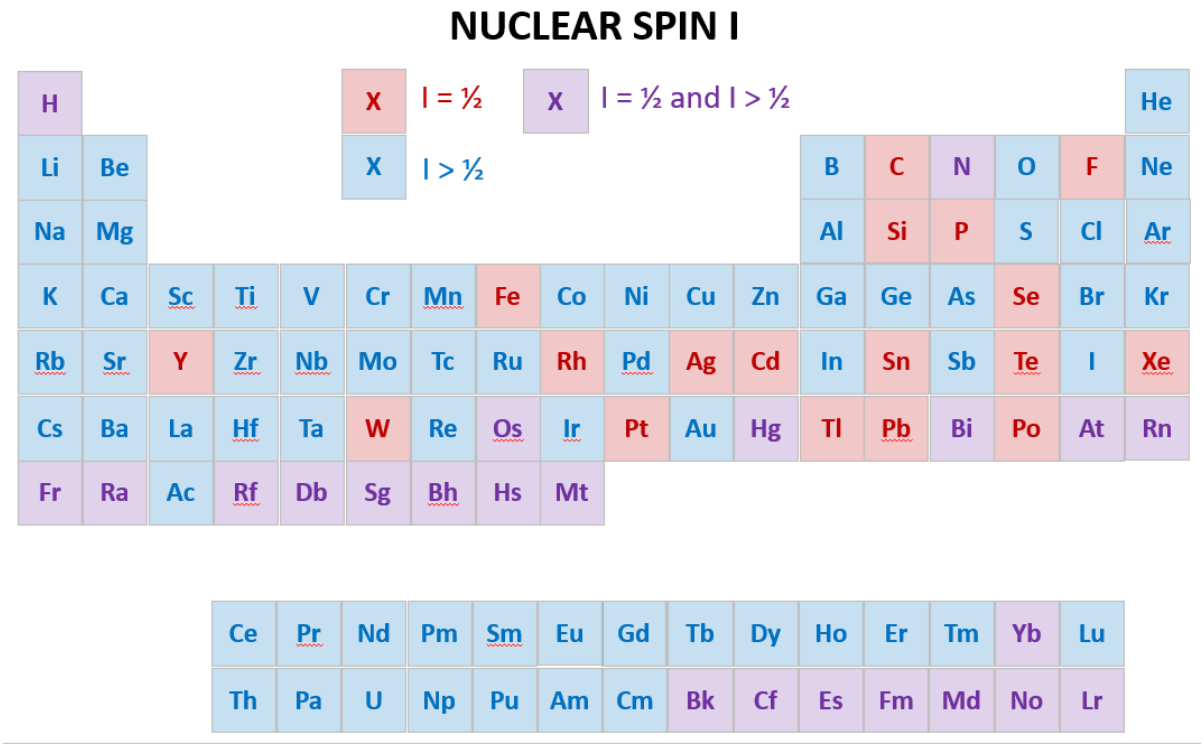

Figure 10: NMR periodic table giving information on the nuclear spin I.

Within the nucleus of an atom, the protons and neutrons can be distributed symmetrically or asymmetrically. If the distribution is symmetric, then the spin *I* of the nucleus is ½ and the interaction with the EFG is independent of direction. However, if the distribution is asymmetric, $I > ½$ and thus the EFG can interact with the nucleus and will result in a certain rotational effect on the nucleus. This exhibited moment is called the quadrupole moment and is represented by *Q*. A non-zero *Q* indicates that the charge distribution is not spherically symmetric (see below).

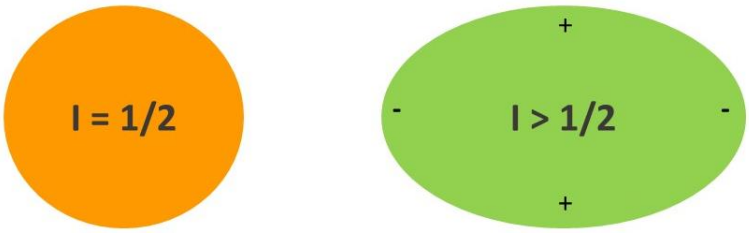

Figure 11: Charge distribution for spherical (I = ½) and non-spherical (I > ½) nuclei.

By convention, the value of Q is positive if the ellipsoid is prolate and negative if it is oblate (see Figure 12). A larger Q value means a stronger interaction between the asymmetric nuclear with the EFG.

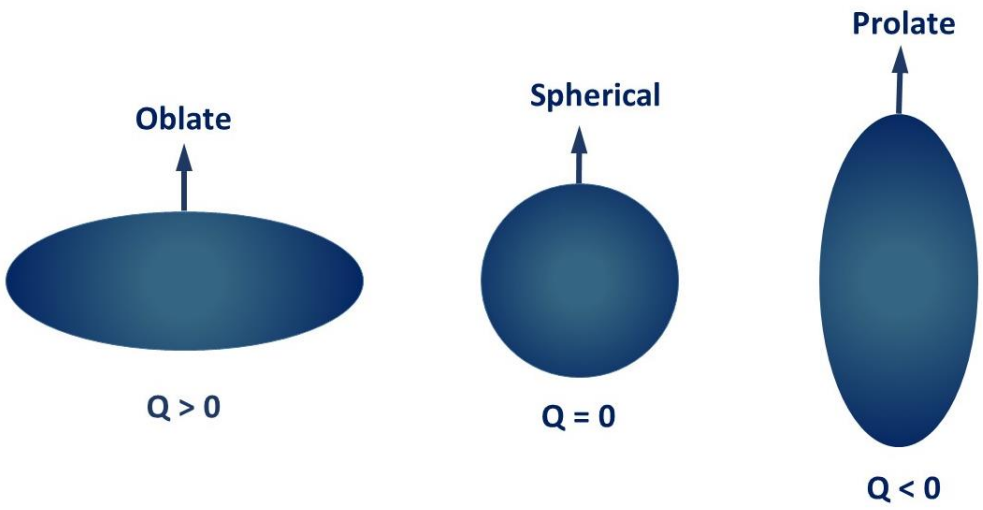

Figure 12: Shapes of oblate, spherical and prolate ellipsoid for charge distribution. The arrows on the shapes indicate the symmetry axis.

2.3 – Electric Field Gradient

The electric field gradient is associated with the change of the electric field that a nucleus will feel or "see" generated by other nuclei in its environment and the electronic charge distribution of a molecule at a particular point in space in which the nucleus in question is

located.[19] The EFG at the nucleus depends both on the electronic structure of the atom itself and also its nearby neighbour atoms. If we take the simple example of a sodium ion in a sodium chloride crystal, one would see an electric field and an EFG for all the neighbouring Na^+ and Cl^- present in the environment. In this special case though, the EFG is zero because the crystal symmetry is cubic. For an EFG to be non-zero, the charge symmetry must be non-spherical in the crystal. In addition, EFGs represent the second derivative of the electrostatic potential and due to that, the EFG is a symmetric tensor with zero trace.[20] More simply this means it can be represented as a physical object: an ellipsoid where off-diagonal elements represent reorientation of the principal axis system. The EFG ellipsoid is on average rhombic and fluctuates both in form and orientation. In molecular species, the EFG estimation is mainly dominated by covalent bonds' polarization and the neighbouring molecules' effects can be neglected. For ionic and atomic species, fluctuations in the EFGs are due to intermolecular forces. The EFG is best described by a second rank tensor, shown below.

$$V = \begin{bmatrix} V_{xx} & V_{xy} & V_{xz} \\ V_{yx} & V_{yy} & V_{yz} \\ V_{zx} & V_{zy} & V_{zz} \end{bmatrix}$$

Figure 13: Representation of the EFG second rank tensor

2.4 – Quadrupolar coupling

In order to understand what quadrupolar coupling is, one must first establish the concept of a quadrupole. Quite simply, a quadrupole can be thought of as two dipoles (a dipole being a bond or molecule having opposite charges on its ends).[21] However, different to a

dipole, the quadrupole will not couple to a symmetric field as the forces and subsequent torques on the quadrupole will cancel. Figure 13 below shows a representation of a quadrupole.

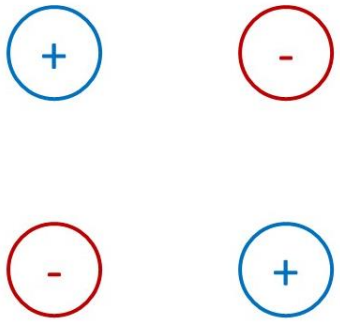

Figure 14: Representation of a quadrupole

Now coming back to the quadrupolar coupling, this is an interaction that occurs in nuclei having more than 2 different spin states. It exists without any applied magnetic field and the energy of corresponding splitting between the different states could be quite strong (kHz to hundreds of MHz).[21] The splitting is what is detected by NQR, nuclear quadrupole resonance, which will be described shortly. It is also important to note that nuclei with spin 0 or ½ do not have this quadrupolar interaction. Only those with a spin greater than ½ have a quadrupolar moment (*Q*) that will interact with the EFG and causes the degeneracy of the nuclear energy levels to be lifted. Due to the 3D nature of a quadrupole it may be described by a second rank tensor *Q*, represented in Figure 15 below.

$$Q = \begin{bmatrix} Q_{xx} & Q_{xy} & Q_{xz} \\ Q_{yx} & Q_{yy} & Q_{yz} \\ Q_{zx} & Q_{zy} & Q_{zz} \end{bmatrix}$$

Figure 15: Representation of the quadrupolar moment Q second rank tensor

The quadrupole can then couple to an EFG, denoted as V, described earlier as a second rank tensor (please refer back to Figure 13). The quadrupolar interaction **Q** can be represented with the following equation,

$$\mathbf{Q} = \frac{eQ\boldsymbol{V}}{2I(2I-1)h}$$

Equation 7. Quadrupolar interaction **Q**

where *Q* is the electric quadrupolar moment, *I* is the spin quantum number, *e* is the charge of the electron and **V** is the EFG given by the following tensor, in the principal axis system (PAS) of the EFG. This comes from one of the numerous definitions associated with the EFG, precisely that $V_{xx} + V_{yy} + V_{zz} = 0$

$$\mathrm{V} = \begin{pmatrix} V_{xx} & 0 & 0 \\ 0 & V_{yy} & 0 \\ 0 & 0 & V_{zz} \end{pmatrix}$$

Figure 16. Representation of the EFG tensor with the conventional labels where the diagonal elements of the EFG are ordered in ascending magnitude.

Also, by convention, the diagonal elements of the EFG are placed in ascending absolute value, such that $|V_{xx}| \leq |V_{yy}| \leq |V_{zz}|$. This allows for the definition of the EFG asymmetry parameter, η, given by the following equation

$$\eta = \frac{V_{xx} - V_{yy}}{V_{zz}}$$

Equation 8. Asymmetry parameter of EFG

The EFG tensor can also be described using another independent parameter: the nuclear coupling constant, C_Q, shown below. C_Q is usually in Hz units and h is Planck's constant.

$$C_Q = \frac{eQV_{zz}}{h}$$

Equation 9. Nuclear coupling constant

2.5 – Nuclear Quadrupolar Resonance

Different methods are used to measure quadrupolar coupling constants (C_Q) depending on the state of the sample of interest. In the solid state, nuclear quadrupolar resonance (NQR) is a standard technique, while in gas phase microwave spectroscopy can be used for small molecules.[20] It is a radiofrequency spectroscopic technique that is used to detect signals from solids containing nuclei with $I > ½$ and having a reasonably high isotopic abundance. The signals arise from the interaction of the electric quadrupole moment of the nuclei with the EFG in the sample. NQR is very similar to NMR (though not as popular and commonly used), but one main difference is that NQR does not require a static magnetic field. Indeed, NQR is based on the interaction between the non-symmetric charge distribution eQ of the nucleus with the nuclear spin $I \geq 1$ and the tensor of the internal EFG while in NMR, it is determined primarily by the interaction of the non-zero nuclear spin $I \geq ½$ with an external magnetic field B_0. NQR measurements can possess high spectral resolution, precision, specificity and speed of measurements. Since resonance frequencies do not depend on the orientation of grains in powder samples, there is more versatility in the type of sample used. Mono-crystals and polycrystalline powder can therefore produce the same sharp NQR lines.[22] NQR is also highly sensitive to small changes in electron density distribution, which provides important

information on the structural and chemical properties of molecules. One reason for the more limited practical application of NQR seems to lie in the lack of equipment.[23] But similarly to NMR spectroscopy once again, the primary goal of NQR is to determine the nuclear transition frequencies and/or the relaxation times and then to relate those to a property of a material being studied.[24] Like NMR, NQR is a quantitative method; the signal intensity is proportional to the number of nuclei with the corresponding resonance frequency.[23] NQR is also used to obtain detailed information on crystal symmetries and bonding, phase transitions in solids and other properties of solid state materials of interest to physicists and chemists. NQR frequencies for various nuclei vary between several kHz and up to 1000 MHz. These values will depend on the quadrupole moments of the nucleus, the valence electrons state and the type of chemical bond between the atom of interest. Using NQR frequencies, the quadrupole coupling constant (C_Q) and asymmetry parameter (η) can be calculated.[25] The common NMR isotopes such as ^{1}H, ^{13}C, and ^{15}N cannot be used since they have a nuclear spin ½. ^{12}C and ^{16}O as well cannot be used either as they have a nuclear spin of zero. Some more common NQR isotopes used are ^{2}H, ^{6}Li and ^{7}Li, ^{14}N, ^{17}O, etc. In this thesis, molecules containing ^{79}Br and ^{81}Br, as well as ^{127}I will be the isotopes of interest.

Some other fields of applications for NQR can be separated into 4 other groups[23]:

1. Studies of electron density distribution in molecules – changes in orbital populations

2. Studies of molecular motions – reorientations, rotations (hindered and non-hindered)

3. Studies of phase transitions

4. Studies of impurities and mixed crystals

2.6 – Density Functional Theory

To understand density functional theory (DFT), one must first know what ab initio methods are. These were developed in order to investigate systems at the nanoscale.[26] The calculations used must remain computationally feasible while ensuring the most accurate model of interactions between atoms.

For a many-electron system, the resolution of the Schrödinger equation $\hat{H}\Psi = E\Psi$ is impossible. Remember that the Schrodinger equation helps in finding the energy of the system (E) and its wavefunction Ψ. The wavefunction Ψ completely describes the state of the system and if Ψ is known, then everything else about the system (energy, orbitals, dipole moment) is also known.[27] But, it is an extremely complicated function as it depends on the time and coordinates of all particles in the system. The Hamiltonian *H* is the total energy operator and can be separated into two mechanics: classical and quantum. Classical will include the kinetic energy = 1/2 mass x $(\text{velocity})^2$ and the momentum = mass x velocity. As for quantum mechanics, there is an operator (prescription of what to do with a wavefunction such as multiply by, divide, take a derivative, etc.) for that and the Hamiltonian for quantum mechanics is equal to the kinetic energy operator for all particles + potential energy. What is complicated about Hamiltonians is due to the many-body interactions in the potential energy term which makes it impossible to solve exactly for systems with 2 or more electrons. Wavefunctions are thus a complicated multi-dimensional function. Therefore, approximated methods such as Hartree-Fock, Monte Carlo and Density Functional Theory, have been implemented. Among these methods, Density Functional Theory, DFT, has become the most popular. More and more work on DFT and its implementation are being realized and DFT has become a standard approach for studying materials. We can only solve the Schrödinger equation exactly for up to

one electron system, so it is clearly not applicable to real life systems, which have multiple and high numbers of electrons.[28] Therefore, in order to solve systems, there needs to be some involvement of approximations and 'tricks'; one of these approximations is the Born-Oppenheimer one. This will lead to the Hohenburg-Kohn theorem. Electron density was introduced to simplify the wavefunction; it takes the probability density function and sum up all of the possibilities covering all space for the electrons. This electron density can be then measured (e.g., X-ray diffraction). The electron density of a system determines all-ground-state properties of the system and in this case the total ground state energy of a many-electron system is a functional of the density. Therefore, if the electron density functional of a system is known, then so is the total energy of the system. Due to this, the electron density is used as a functional and all other ground state properties are then calculated. In DFT, the Schrödinger equation is solved by using electron density instead of the wave function and this simplifies the calculations a lot.[29]

Exchange correlation is an approximation that takes care of all the quantum mechanical information. Remember that two electrons interact not only via their electronic charge, but also by their spins. Mutual repulsion and attraction will occur. In order to properly conduct calculations, one must choose the adequate functional for their work. Therefore, which functional should you choose for your work? If the system is composed of small molecules, then the one-line answer is either B3LYP or B3PW. B3LYP is the most widely used functional and has a superior performance in energy assessments B3LYP will be described more in the next section. It is important to note that there is no presently existing functional that is highly accurate enough for all properties of interest. Since no functional is 100% accurate, it is better to match and compare some experimental data with results in order to choose the proper

functional. As shown in Figure 17, there is always a compromise between XC functionals; If the results need to be very accurate, then the functional used must be complex and therefore time consuming. If a simple functional is used, it will be quick to do but the results will not be very accurate.

Figure 17: Relation and compromise between accuracy and simplicity of exchange correlation functionals.

Finally, DFT is a helpful tool used to calculate properties of atoms and molecules such as the structure, energy, orbitals/electronic structure, reactivity (Gibbs energies) and spectroscopic properties such as NMR, IR and UV-Vis spectra.[27]

2.7 – Theoretical models

A theoretical model or method is a way to model a system using a specific set of approximations. These approximations are then combined with calculation algorithms and applied to atomic orbitals (defined by the basis set). This will allow the computation of molecular orbitals and energy.[30]

In general, these methods can be separated into 4 main types: semiempirical, ab initio, density functional, molecular mechanics. Selecting one of these theoretical methods depends on the size of the system and on the level of approximation.

B3LYP is a hybrid functional developed in the 80s that contains elements from both DFT and Hartree-Fock (HF) theory. It includes exact electron exchange as well as GGA (generalized gradient approximation, where electron density variation is taken into account) and LDA (local density approximation) that assumes that electron density variations are slow and treat the local density as a uniform electron gas. B3 is Becke's 3 parameter exchange correlation functional which uses 3 parameters to mix in the exact Hartree-Fock exchange correlation and LYP is the Lee Yang and Parr correlation. It is one of the most used methods and for many reasons; B3LYP is generally faster than HF techniques while yielding comparable results and it is robust for a DFT method. It is also not as heavily parameterized as other hybrid functionals (has only 3 parameters whereas others can go up to 20 some).

Basis Sets

Selecting a proper basis set for a computational job is very important. Why is that? A basis set is a set of wave functions that describes the shape of atomic orbitals (AOs). Molecular orbitals (MOs) are computed using the selected theoretical model by linearly combining the AOs (also known as LCAO). Its selection can be influenced by the size of the system being studied and also on the computing resources that are available. Generally, it is desirable to use the smallest basis set that produces the most reliable and accurate results. Research has shown that choosing an appropriate basis set is more important than choosing the method.[31] The basis set chosen will be directly affecting the level of calculation approximation. The more accurate the results are, the more CPU time it will require.

There are two types of orbitals; Slater type orbitals (STOs) and Gaussian type orbitals (GTOs). Though STOs have a better description of the shape of atomic orbitals, GTOs' remarkable advantage is that they are much easier to compute. Just to give an example, it is

faster to compute many GTOs and combine them together than to compute a single STO. This is why combinations of GTOs are commonly used to describe STOs, which in turn, describe AOs.

In this work, the 6-311G(3df) and DGDZVP basis set were used. The first one were for ^{14}N, ^{17}O, whereas the latter was used for ^{127}I and ^{79}Br. 6-311G is typically used for first row atoms (or for atoms H through Zn to be more precise), 3df is included for diffuse functions at the d and f level (3 sets of polarization d-functions and one set of polarization f-functions are added to heavy atoms). The 6-311G is a Pople basis set and is a *split-valence* basis set. Its notation is typically *X-YZg*, where *X* represents the number of primitive Gaussians (core atomic orbital basis function), *Y* and *Z* indicate that the valence orbitals are composed of two basis functions each, one being a linear combination of *Y* primitive Gaussian functions and the other being also a linear combination but with *Z* primitive Gaussian functions. In the case of *X-YZg*, since there are only two numbers (*Y* and *Z*) after the hyphen, this represents a *split-valence double-zeta* basis set. In the case of 6-311G, there are three numbers so this would be a *split-valence triple-zeta* basis set. In general, *triple-zeta* and *quadruple-zeta* basis sets are more accurate than *double-zeta* ones, but require more time to perform. The DGDZVP basis set, on the other hand, has been shown to perform much better than *double-zeta* and even *triple-zeta* basis set in estimating halogen-bond strengths.[32] Since it has a small size as well, it is well-suited for studying halogen bonding in large systems and its accuracy was also an advantage compared to the other basis sets. No diffuse function is available with DGDZVP but it proved to be not necessary since just by itself it performed very well. In principles and for methods other than DGDZVP, diffuse functions should improve the results. These quite shallow Gaussian basis functions are a common addition to basis sets and more accurately represent

the “tail” part of atomic orbitals that are distant from the centre of the atomic nucleus. These additions can be important and considerable for anions and other large molecular systems.

2.8 – Natural Bonding Orbitals (NBOs)

Natural bond orbitals (NBOs) are used in computational chemistry to calculate the distribution of the electron density in the bonds and atoms. They are localized few-centre (usually 1 or 2, but occasionally more) orbitals describing the molecular bonding pattern of individual or pairs of electron in an optimal compact form.[33] More precisely, NBOs are an orthonormal set of localized “maximum occupancy” orbitals with N/2 members give the most accurate possible Lewis-like structure of the total N-electron density.[33] It is important to note that neither the form, locations of the localized bonds nor the lone pairs of electrons are pre-determined. Instead, a computer NBO program searches all the possible ways of drawing the bonds and lone pairs with a varying optimal bonding pattern which with place maximum electron occupancy (highest percentage of the total density) in the leading N/2 Lewis-type NBOs, which is typically the case for more than 99% of common organic molecules.[33]

Chapter 3 – Solid-state multinuclear magnetic resonance and X-ray crystallographic investigation of the phosphorus···iodine halogen bond in a (dicyclohexylphenylphosphine)(1,6-diiodoperfluorohexane) cocrystal

Authors: D. N. Zheng, P. M. J. Szell, S. Khiri, J. S. Ovens, and D. L. Bryce

Statement of Authenticity. I certify that I have prepared the following article featuring my own work and Dr. Patrick J. Szell's work with guidance from my supervisor, Dr. David Bryce. Dr. Patrick Szell is acknowledged for his help with the manuscript and figures along with his assistance with NMR experiments. Dr. David Bryce is acknowledged for support, guidance and contributions to the manuscript. Dr. Jeffrey Ovens is acknowledged for acquiring and solving the crystal structures presented in the article.

Permissions. I declare that I have obtained permission from the coauthors to include this article in my thesis. Chapter 3 has been accepted for publication in Acta Cryst B. in April 2022.

Abstract. Halogen bonding to phosphorus atoms remains uncommon, with relatively few examples reported in the literature. Here, the preparation and investigation of the cocrystal (dicyclohexylphenylphosphine)(1,6-diiodoperfluorohexane) by X-ray crystallography and solid-state multinuclear magnetic resonance spectroscopy is described. The crystal structure features two crystallographically unique C-I···P halogen bonds ($d_{I\cdots P}$ = 3.090(5) Å, 3.264(5) Å) and crystallographic disorder of one of the 1,6-diiodoperfluorohexane molecules. The first of these is the shortest and most linear I···P halogen bond reported to date. ^{13}C, ^{19}F, and ^{31}P magic-angle spinning solid-state NMR spectra are reported. A ^{31}P chemical shift change of -7.0 ppm in the cocrystal relative to pure dicyclohexylphenylphosphine, consistent with halogen bond formation, is noted. This work establishes iodoperfluoroalkanes as viable halogen bond donors when paired with phosphorus acceptors, and also shows that dicyclohexylphenylphosphine can act as a practical halogen bond acceptor.

Keywords: **cocrystal; halogen bonding; solid-state NMR; crystallographic disorder**

1. Introduction

The halogen bond is a non-covalent attractive interaction between the electrophilic region of a halogen atom, named the σ-hole, and an electron-rich site.(Cavallo *et al.*, 2016; Gilday *et al.*, 2015; Berger *et al.*, 2015; Bulfield & Huber, 2016; Li *et al.*, 2016) The σ-hole is associated with a region of depleted electron density along the extension of the R–X bond (X = halogen),(Clark *et al.*, 2007) with the magnitude of the σ-hole increasing with the size of the halogen. The halogen bond exhibits several advantageous features, such as the tuneability of the interaction strength (Riley *et al.*, 2011, 2013) and its linearity. Consequently, the halogen bond has found applications in ligand & anion binding,(Ungati *et al.*, 2018; Abate *et al.*, 2009; Brown & Beer, 2016; Langton *et al.*, 2014; Decato *et al.*, 2020) synthesis,(Bulfield & Huber, 2016; Tepper & Schubert, 2018; Jungbauer & Huber, 2015) crystal engineering,(Aakeröy *et al.*, 2015; Metrangolo *et al.*, 2005) and functional materials.(Priimagi *et al.*, 2013; Christopherson *et al.*, 2018; Berger *et al.*, 2015)

Cocrystals are multi-component crystalline solids and have been shown to be versatile in studying the influence of the halogen bond on local physicochemical properties. Cocrystals featuring the halogen bond can be prepared using traditional solvent techniques, e.g. slow evaporation, and can also be prepared through solvent-free methods, such as mechanochemistry, and cosublimation. (Carstens *et al.*, 2019; Szell, Gabriel, *et al.*, 2018) Mechanochemistry *via* ball milling is a rapid and convenient method of preparing halogen bonded cocrystals, while also reducing the environmental footprint through the reduction in solvent usage.(Cinčić *et al.*, 2008b; Lisac *et al.*, 2018; Eraković *et al.*, 2018; Cinčić *et al.*, 2008a) Mechanochemistry using a ball mill consists of grinding two or more compounds together in a jar in the presence of grinding balls.(Braga *et al.*, 2013; Fischer *et al.*, 2016) Solid-

state NMR is well suited as an analytical technique for investigating solids featuring the halogen bond,(Xu *et al.*, 2020; Vioglio *et al.*, 2016) such as cocrystals obtained from mechanochemical preparations,(Morin *et al.*, 2019; Szell, Dragon, *et al.*, 2018) providing clear changes in chemical shifts,(Cerreia Vioglio *et al.*, 2016; Viger-Gravel *et al.*, 2013; Viger-Gravel *et al.*, 2011; Gao *et al.*, 2012; Pérez-Torralba *et al.*, 2014) quadrupolar coupling constants,(Szell & Bryce, 2016; Cerreia Vioglio *et al.*, 2018; Szell, Grebert, *et al.*, 2019; Viger-Gravel, Leclerc, *et al.*, 2014; Szell, Cavallo, *et al.*, 2018) *J*-coupling constants,(Viger-Gravel, Meyer, *et al.*, 2014; Xu *et al.*, 2015) dipolar coupling constants,(Weingarth *et al.*, 2008) and dynamics.(Szell, Zablotny, *et al.*, 2019; Lemouchi *et al.*, 2011; Catalano *et al.*, 2015; Catalano *et al.*, 2017)

The C-I···P halogen bond moiety has remained somewhat elusive due in part to the reactivity of the phosphorus atom,(Garabadzhiu, Kuznetsov, *et al.*, 1979; Garabadzhiu *et al.*, 1980; Garabadzhiu, Shibaev, *et al.*, 1979) with the first engineered crystal structures featuring this moiety only being recently reported.(Xu *et al.*, 2018; Lisac *et al.*, 2019; Siegfried *et al.*, 2020) Understanding the C-I···P interaction and its preparation can expand the repertoire of halogen bonds, which could allow crystal engineers to include phosphine molecules in new solid forms. Here, we report a new cocrystal composed of dicyclohexylphenylphosphine and 1,6-diiodoperfluorohexane, henceforth referred to as **1a**, as shown in Figure 18. Sample **1a** was investigated using a combination of X-ray crystallography and solid-state multinuclear (^{13}C, ^{19}F, and ^{31}P) magnetic resonance spectroscopy. While X-ray crystallography allows us to directly observe the geometrical parameters of the halogen bond, solid-state NMR experiments allow us to confirm the structure of the powdered solid and to investigate the influence of the halogen bond on the isotropic chemical shifts. Part of the novelty of this work

lies in establishing the validity of using a non-aromatic perfluorodiiodoalkane as a halogen bond donor to phosphorus, as previous sparse reports of halogen bonds to phosphorus in cocrystalline systems have involved only the now iconic perfluoroiodobenzenes. (Xu *et al.*, 2018; Lisac *et al.*, 2019; Siegfried *et al.*, 2020) Further, the dicyclohexylphenylphosphine molecule is used as a halogen bond acceptor for the first time. The application of ^{13}C and ^{19}F solid-state NMR spectroscopy to assess halogen bonding in systems featuring phosphorus-iodine halogen bonds is also reported here for the first time.

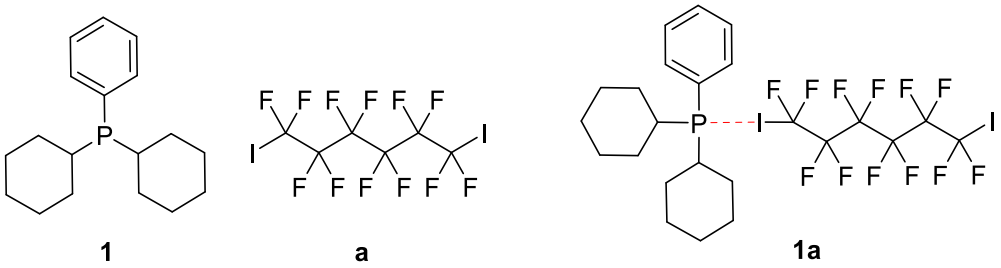

Figure 18 **(a)** Molecular structures of **1** (dicyclohexylphenylphosphine), **a** (1,6-diiodoperfluorohexane), and cocrystal **1a** [(dicyclohexylphenylphosphine)(1,6-diiodoperfluorohexane)] under investigation in this study. The dashed red line in **1a** denotes the C-I···P halogen bond.

2. Experimental

Sample preparation. To a 5 mL stainless grinding jar, 50 mg (0.18 mmol) of dicyclohexylphenylphosphine, 21 μL (0.09 mmol) of 1,6-diiodoperfluorohexane, 25 μL of acetonitrile, and two 5 mm stainless steel grinding balls were added. The grinding jar was sealed and placed in a Retsch MM400 ball mill and milled at a frequency of 25 Hz for 30 minutes at room temperature. **1a** was obtained as a fine white powder (melting point = 96-98°C) and used without further treatment or purification for the solid-state NMR and powder X-ray diffraction experiments. Single crystals were grown by dissolving 20 mg of **1a** in a minimal amount of hexane, approximately 2 mL, and allowing the solvent to evaporate at room temperature for 4 days, yielding colourless crystals. The powder X-ray diffraction was performed on a Rigaku Ultima IV powder diffractometer at room temperature (Cu $K\alpha_1$, λ = 1.54056 Å), scanning from 5° to 55° (2θ range) in increments of 0.02° with a scan rate of 0.8°/minute.

Single-crystal X-ray diffraction. Crystallographic data were collected from a single crystal mounted on a MiTeGen MicroMount using parabar oil. Data were collected on a Bruker Kappa ApexII single crystal diffractometer equipped with a sealed tube Mo K$\boldsymbol{\alpha}$ source ($\boldsymbol{\lambda}$= 0.71073 Å), a TRIUMPH monochromator, and an ApexII CCD detector. Samples were held at 203(2) K using a dry compressed air cooling system. Raw data collection and processing were performed with the Apex3 software package from Bruker.(Bruker, 2010) Initial unit cell parameters were determined from 36 data frames from select $\boldsymbol{\omega}$ scans. Semi-empirical absorption corrections based on equivalent reflections were applied.(Blessing, 1995) Systematic absences in the diffraction data-set and unit-cell parameters were consistent with the assigned space group. The initial structural solutions were determined using ShelxT direct

methods,(Sheldrick, 2008) and refined with full-matrix least-squares procedures based on F2 using ShelXL and ShelXle.(Hubschle *et al.*, 2011) Hydrogen atoms were placed geometrically and refined using a riding model. The CIF file was deposited in the Cambridge Structural Database(Groom *et al.*, 2016) with deposition number 2128052.

^{13}C solid-state NMR. The ^{13}C solid-state NMR experiments were performed at 9.4 T ($\nu_L(^1H)$ = 400.18 MHz) using a Bruker Avance III console and a Bruker 4 mm HXY MAS NMR probe. A $^1H \rightarrow {}^{13}C$ cross-polarization pulse sequence was used, with a 2.5 μs ^{1}H $\pi/2$ pulse followed by a 2 ms contact time using a ramped-contact pulse.(Metz *et al.*, 1994) Samples were packed in a 4 mm zirconium oxide rotor, and the MAS rate was set to 10 kHz. SPINAL64 ^{1}H decoupling(Fung *et al.*, 2000) at a nutation frequency of 100 kHz and a recycle delay of 30 s was used, collecting 4892 scans for **1a** and 2048 scans for **1**. Chemical shifts were referenced relative to tetramethylsilane using the carbonyl peak of α-glycine as a secondary reference at 176.5 ppm.

^{31}P solid-state NMR. The ^{31}P solid-state NMR experiments were performed at 9.4 T ($\nu_L(^1H)$ = 400.32 MHz) using a Bruker Avance III console and a Bruker 4 mm HXY MAS NMR probe. A $^1H \rightarrow {}^{31}P$ cross-polarization pulse sequence was used, with a 4 μs ^{1}H $\pi/2$ pulse followed by a 4.5 ms contact time using a ramped-contact pulse.(Metz *et al.*, 1994) Samples were packed in a 4 mm zirconium oxide rotor, and the MAS rate was set to 9 kHz. Proton decoupling at a nutation frequency of 62.5 kHz and a recycle delay of 2 s was used, collecting 24576 scans for **1a** and 302 scans for **1**. Chemical shifts were referenced using ammonium dihydrogen phosphate at 0.81 ppm.(Bryce *et al.* 2001)

^{19}F solid-state NMR. The ^{19}F NMR experiments were performed at 4.7 T ($\nu_L(^{19}F)$ = 188.27 MHz) using a Bruker Avance III console and a Bruker 2.5 mm HXY MAS NMR probe. **1a**

was packed in a 2.5 mm zirconium oxide rotor, and the MAS rate was set to 25 kHz. A ^{19}F one-pulse experiment was used with a 3.3 μs ^{19}F π/2 pulse, and 128 transients were collected. Chemical shifts were referenced to powdered Teflon at -122 ppm.

3. Results and Discussion

3.1 - X-ray crystallography

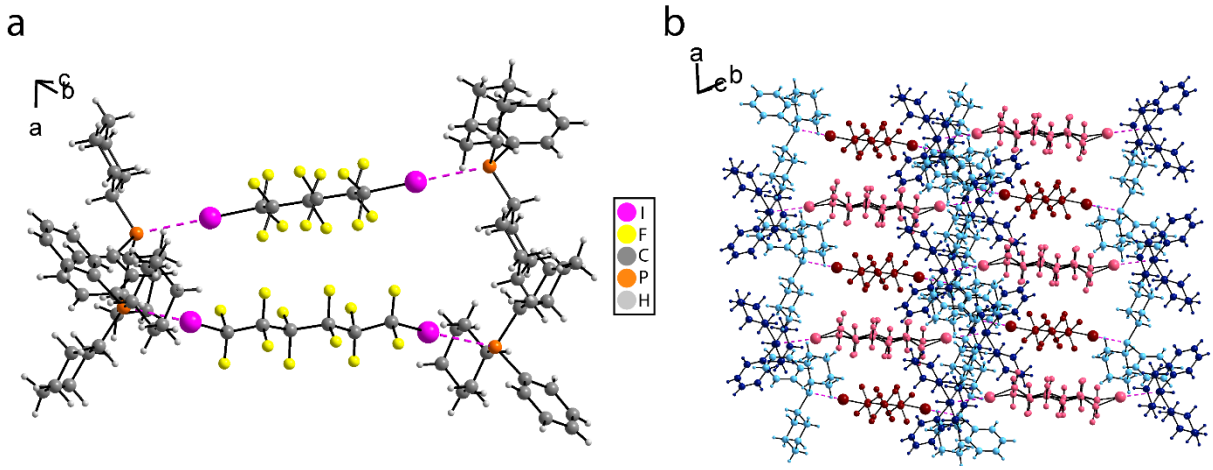

Figure 19 (**a**) Depiction of the crystal structure of **1a**. The C-I···P halogen bond is represented by the dashed magenta line and the crystallographic disorder is not shown here for clarity. (**b**) Depiction of the crystal packing in **1a**. The halogen donor, **a,** is shown in burgundy & pink, while the halogen acceptor, **1**, is shown in dark blue and light blue. The crystallographic disorder for one of the molecules of **a** is shown.

The crystal structure of **1a** features two molecules of **1** and two half-molecules of **a** (*Z* = 2), overall in a 2:1 stoichiometric ratio (Table 2). Two unique C-I···P halogen bonds are observed, with bond geometries of $d_{I\cdots P}$ = 3.090(5) Å and $\theta_{C\text{-}I\cdots P}$ = 178.4(5)° for the P1···I1 halogen bond, and $d_{I\cdots P}$ = 3.264(5) Å and $\theta_{C\text{-}I\cdots P}$ = 167.6(7)° for the P2···I2B halogen bond. These halogen bonds may also be characterized by reduced distance parameters ($R_{XB} = d_{I\cdots P}$ /

Σ_{vdW}) of 0.78 and 0.83, respectively, with the stronger, shorter halogen bond also being more linear. The molecule of **a** comprising atom I2B is disordered over two positions of occupancy, and was solved using a split-site model with an occupancy ratio of 0.47:0.53, while the second molecule of **a** was solved using a single-site model albeit with large thermal ellipsoids (see Figure S1 of the Supporting Information). As shown in Figure 19a, the crystal structure of **1a** features one molecule of **1** at each end of molecule **a**, forming two unique discrete entities that each resemble a dumbbell. As shown in Figure 19b, these discrete halogen-bonded entities are nearly perpendicular to each other and stack side-by-side to form the crystal **1a**.

The phosphorus-iodine halogen bonds in **1a** may be discussed in the context of the small dataset available for other cocrystals featuring such interactions. (Xu *et al.*, 2018; Lisac *et al.*, 2019; Siegfried *et al.*, 2020) For example, a cocrystal of triphenylphosphine with 1,3,5-trifluoro-2,4,6-triiodobenzene which crystallizes in the $P\bar{1}$ space group features only a single crystallographically distinct halogen bond characterized at 200 K by a I···P distance of 3.376(1) Å, a C-I···P angle of 165.26(9)°, and a reduced distance parameter of 0.857.(Xu *et al.*, 2018) Lisac *et al.* (2019) reported similar parameters for a cocrystal of the same composition, but studied at 103 K: a I···P distance of 3.3133(5) Å, a C-I···P angle of 165.33(4)°, and a reduced distance parameter of 0.877. Siegfried *et al*. (2020) provided crystallographic data at 153 K for three different cocrystals of bis(diphenylphosphino)ethane (dppe) with 1,4-diiodoperfluorobenzene, i.e., two different polymorphs with a 1:1 stoichiometry and a third cocrystal with a 1:3 dppe:1,4-diiodoperfluorobenzene stoichiometry. In these three systems, the I···P distance ranges from 3.1732(5) to 3.251(2) Å, the C-I···P angle ranges from 169.97(5)° to 172.930(9)°, and the reduced distance parameter ranges from 0.844 to 0.860. Siegfried *et al*. (2020) also tabulate some longer I···P contacts found in the

literature, namely 3.491(1) Å in ((8-iodo-1-naphthyl)methyl)(phenyl)phosphine (Anderson *et al.*, 2008) and 3.289(1) Å in bis(7-iodo-2,3-dihydrothieno[3,4-b][1,4]dioxin-5-yl)(phenyl)phosphine. (Tusy et al., 2014). Thus, it is evident that one of the two I···P halogen bonds in **1a** is the shortest and most linear reported to date in the literature (3.090(5) Å; 178.4(5)°). The other halogen bond in **1a** is characterized by geometrical parameters more typical of previous examples in the literature (3.264(5) Å and 167.6(7)°).

Table 2: Summary of the crystallographic parameters for the crystal structure of **1a**

CCDC number	2128052
Crystal data	
Chemical formula	$2(C_{18}H_{27}P)\cdot(C_6F_{12}I_2)$
M_r	1102.59
Crystal system, space group	Triclinic, *P*1
Temperature (K)	293
a, *b*, *c* (Å)	10.321 (3), 15.231 (4), 15.663 (4)
α, β, γ (°)	82.730 (6), 80.201 (5), 71.847 (6)
V (Å^3)	2298.5 (11)
Z	2
Radiation type	Mo *K*α
μ (mm^{-1})	1.52
Crystal size (mm)	0.13 × 0.09 × 0.05
Data collection	
Diffractometer	Bruker *APEX*-II CCD
Absorption correction	Multi-scan *SADABS*
T_{min}, T_{max}	0.604, 0.745
No. of measured, independent and observed [$I > 2\sigma(I)$] reflections	19267, 6489, 3224
R_{int}	0.099
θ_{max} (°)	23.3
$(\sin\theta/\lambda)_{max}$ (Å^{-1})	0.556
Refinement	
$R[F^2 > 2\sigma(F^2)]$, $wR(F^2)$, S	0.123, 0.192, 1.08
No. of reflections	6489
No. of parameters	605
No. of restraints	259
H-atom treatment	H-atom parameters constrained
	$w = 1/[\sigma^2(F_o^2) + 37.981P]$ where $P = (F_o^2 + 2F_c^2)/3$
$\Delta\rho_{max}$, $\Delta\rho_{min}$ (e Å^{-3})	1.13, −1.21

Computer programs: Bruker *APEX3*, Bruker *SAINT*, *SHELXT* 2014/5 (Sheldrick, 2014), *SHELXL2018*/3 (Sheldrick, 2018).

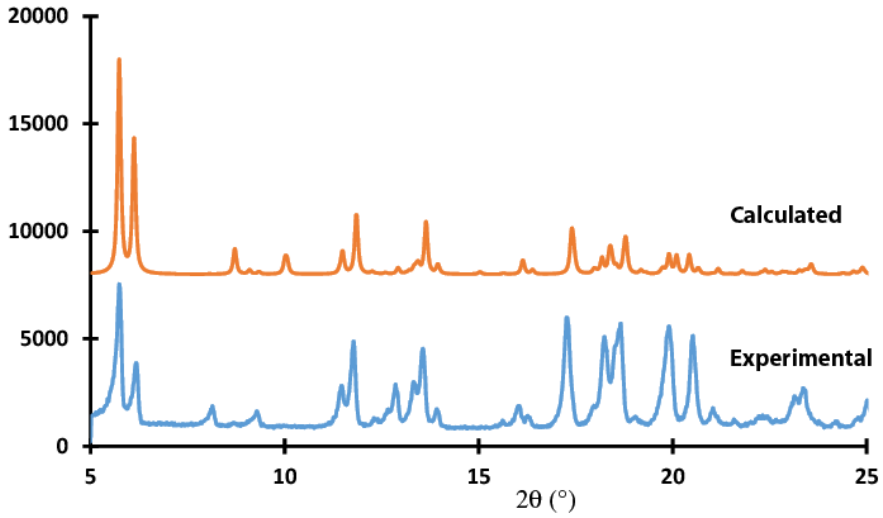

Figure 20: Experimental (blue, below) and calculated (orange, above) powder X-ray diffractograms of compound **1a**.

Shown in Figure 20 are experimental and calculated powder X-ray diffractograms of **1a**. The agreement between the experimental trace and that computed on the basis of the single crystal structure indicates that the crystal phase in the powder form agrees with that determined from the single-crystal X-ray structure determination. Broadening and slight shifts in some peaks of the experimental diffractogram are well-known and attributed to particle size effects, possible strain effects, and instrumental conditions.(Ungár, 2001; King and Payzant, 2001) The PXRD data thus presently provide a valuable check to ensure that the powders studied by solid-state NMR spectroscopy (*vide infra*) are representative of the single-crystal structure and that the NMR data may therefore be confidently interpreted in the context of this structure.

3.2 - Solid-State NMR Spectroscopy

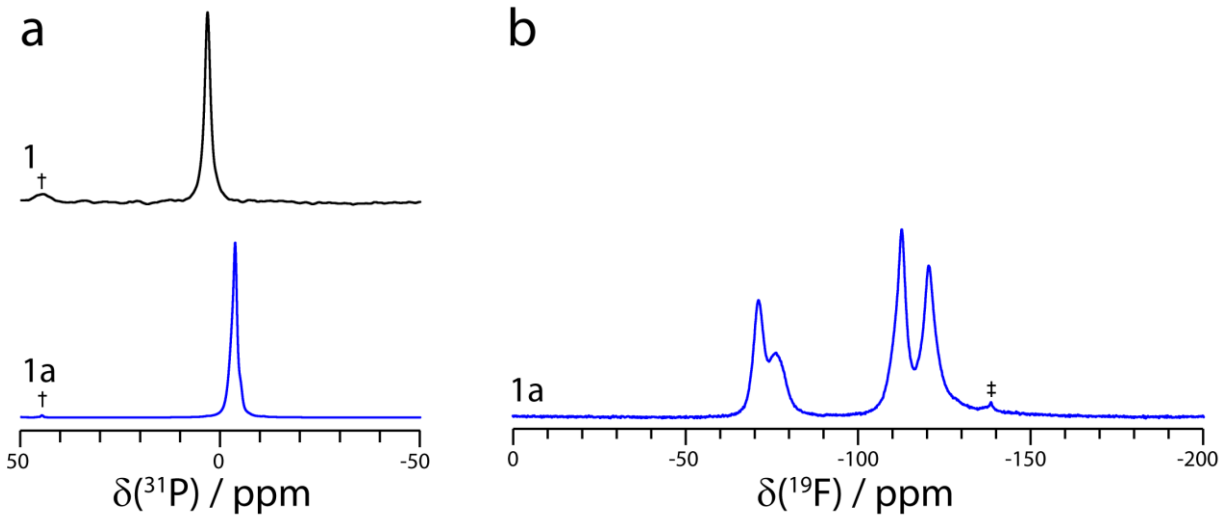

Figure 21 **(a)** Experimental ^{31}P cross-polarization magic-angle spinning solid-state NMR spectra of **1** (above, black) and cocrystal **1a** (below, blue) acquired at B_0 = 9.4 T (ν_{MAS} = 9 kHz). The dagger indicates a trace amount of impurity, assigned to dicyclohexylphenylphosphine oxide. **(b)** Experimental ^{19}F magic-angle spinning solid-state NMR of cocrystal **1a** acquired at B_0 = 4.7 T (ν_{MAS} = 25 kHz). The double-dagger denotes a trace amount of impurity.

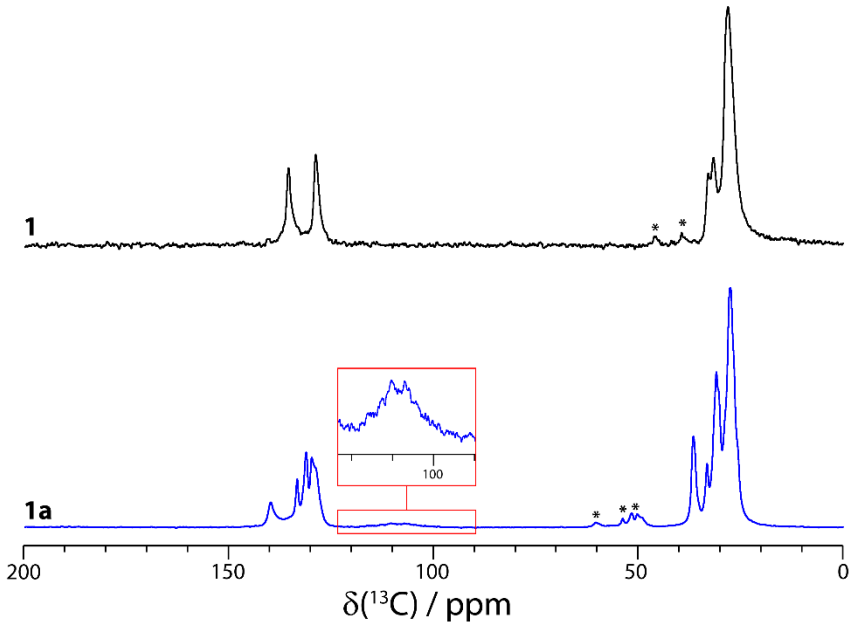

Figure 22 Experimental $^{1}H \rightarrow {}^{13}C$ cross-polarization magic-angle spinning solid-state NMR spectrum of **1** (top, black; ν_{MAS} = 9 kHz) and cocrystal **1a** (bottom, blue; ν_{MAS} = 8 kHz) acquired at B_0 = 9.4 T. The asterisks denote spinning sidebands while the inset in red shows the lower intensity resonance assigned to the iodinated (CF_2I) carbon.

Solid-state NMR spectroscopy has a long history of providing structural and crystallographic information.(Harris *et al.*, 2009; Bryce and Taulelle, 2017) The field of NMR crystallography, which harnesses the synergies between diffraction and spectroscopy, has developed substantially in recent years to the point where complete crystallographic structures may now be routinely solved using some combination of powder X-ray diffraction data, experimental NMR data, and computational chemistry.(Hodgkinson, 2020; Engel *et al.*, 2019) More rudimentary uses of solid-state NMR in the analysis of the structure of powders and crystals include verifying phase purity, assessing the correct space group, identifying the

number of distinct molecules in the asymmetric unit, and providing evidence for new crystal phases, polymorphs, cocrystallization, etc. (Martineau *et al.*, 2014) Solid-state NMR is also invaluable for identifying and characterizing amorphous phases, guest species, and dynamic processes in powders and crystals.(Xu *et al.*, 2016)

As shown in Figure 21a, the ^{31}P solid-state NMR spectrum of **1a** displays a single resonance at a chemical shift of $\delta(^{31}P)$ = -3.9 ppm, which is 7.0 ppm lower than that of **1** (Table 2). The ^{31}P NMR line shape of **1a** features a slight broadening and a chemical shift change that is consistent with that observed in prior ^{31}P NMR spectra of the C-I⋯P moiety in a (triphenylphosphine)(1,3,5-trifluoro-2,4,6-triiodobenzene) cocrystal.(Xu *et al.*, 2018) While the crystal structure of **1a** has Z' = 2 and two resonances are expected in the ^{31}P spectrum, the broadened features observed in the experimental ^{31}P line shape may be due in part to two overlapping ^{31}P resonances, along with the presence of crystallographic disorder. The presence of a minor impurity at $\delta(^{31}P)$ = 44.6 ppm has been assigned to dicyclohexylphenylphosphine oxide.

As shown in Figure 21b, the ^{19}F NMR spectrum also features broadening of all the resonances, attributable to crystallographic disorder and homonuclear ^{19}F-^{19}F dipolar couplings. As the starting material **a** is a liquid at room temperature, ^{19}F solid-state NMR was not performed. The mere fact that it was possible to record a ^{19}F solid-state NMR spectrum for the product **1a** is therefore direct evidence of halogen-bond-induced cocrystal formation. $^{19}F \rightarrow {}^{31}P$ cross-polarization magic-angle spinning NMR experiments also unequivocally establish halogen-bond-induced cocrystal formation.

To date, ^{13}C solid-state NMR spectroscopy has not been used to characterize cocrystals featuring iodine-phosphorus halogen bonds. ^{13}C NMR could prove to be a useful indirect tool to monitor halogen-bond-induced cocrystallization in such systems, despite the indirect role that carbon plays in such bonds. As shown in Figure 22, the ^{13}C solid-state NMR spectrum of **1a** displays multiple resonances, and those associated with the perfluorinated halogen bond donor, **a**, can be observed (Table 3). The lower intensity of the resonances assigned to **a** are due in part to the smaller ^{1}H-^{13}C dipolar coupling, reducing the cross-polarization efficiency, along with the presence of ^{13}C-^{19}F couplings, and in the case of the C-I carbon, ^{13}C-^{127}I couplings.(Terskikh *et al.*, 2009) The ^{13}C chemical shifts of **1a** are distinct from those of **1**, and much like in the ^{31}P and ^{19}F spectra, the ^{13}C resonances feature broadening. This broadening may be in part due to the crystallographic disorder and unfortunately precludes the confirmation of *Z*' by solid-state NMR.

Table 3 Experimental ^{31}P, ^{19}F, and ^{13}C solid-state NMR isotropic chemical shifts measured for **1** and **1a** (all in ppm).

Nucleus	**1**	**1a**
^{31}P	3.1	-3.9
^{19}F	n/a	-71.2, -76.3, -112.7, -120.5
^{13}C	27.9, 31.4, 32.8, 128.6, 135.2	27.4, 30.8, 33.1, 36.4, 108.6, 129.6, 130.9, 133.1, 139.6

Conclusions

A novel cocrystal **1a**, (dicyclohexylphenylphosphine)(1,6-diiodoperfluorohexane), was prepared by mechanochemical ball milling and investigated using a combination of X-ray crystallography and ^{31}P, ^{19}F, and ^{13}C solid-state NMR spectroscopy. The single-crystal X-ray crystal structure reveals the presence of two crystallographically distinct C-I···P halogen bonds, and the solid-state NMR results support the occurrence of cocrystallization. One of the two halogen bonds is the shortest and most linear observed to date for a I···P interaction, and is characterized by a reduced distance parameter of 0.78. The ^{31}P isotropic chemical shift of the dicyclohexylphenylphosphine moiety decreases by 7.0 ppm upon formation of the phosphorus-iodine halogen bond. In addition, further synergies between diffraction and NMR strengthened the characterization of **1a**. These include cocrystallization-induced ^{13}C chemical shifts of remote donor and acceptor carbon atoms; the observation of a ^{19}F NMR signal indicative of cocrystal formation rather than physical mixing of the two pure component molecules; and peak broadening consistent with a crystalline product featuring internal disorder of the iodoperfluoroalkane moiety.

This work contributes to a growing body of knowledge concerning cocrystal engineering with phosphorus as a halogen bond acceptor. In particular, the use of iodoperfluoroalkanes as halogen bond donors which interact with phosphorus-based acceptors has been established. The dicyclohexylphenylphosphine molecule has also been shown to act as a halogen bond acceptor for the first time. One can thus envision the future use of a broader range of phosphine molecules as halogen bond acceptors and indeed as acceptors for various other classes of element-based electrophilic non-covalent interactions such as chalcogen bonds, pnictogen bonds, and tetrel bonds.

Acknowledgements

The authors thank Dr. Peter Pallister from the University of Ottawa for experimental solid-state NMR support. D.L.B. thanks NSERC for research funding.

Supporting information

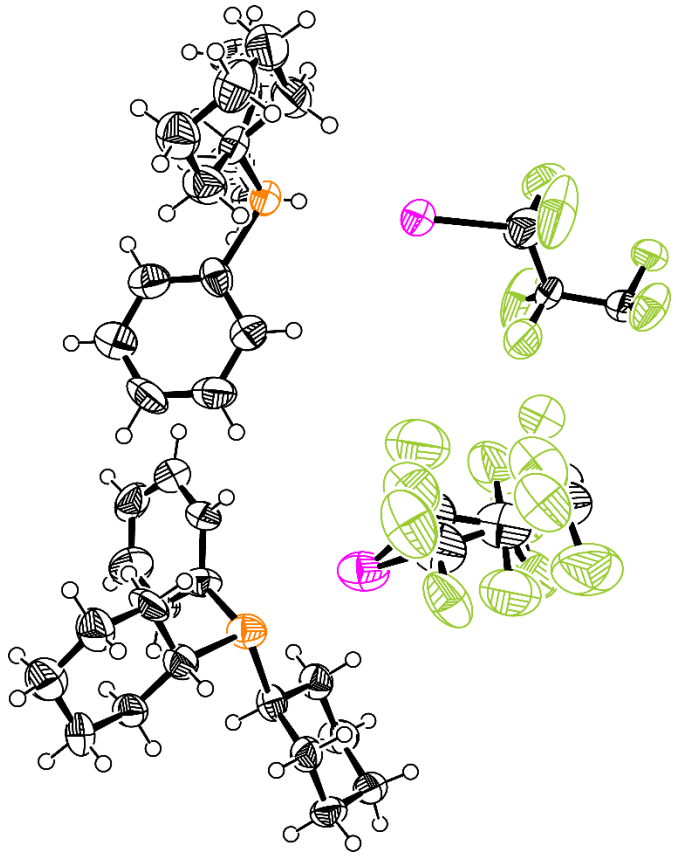

Figure S1 Thermal ellipsoid plot of the crystal structure of **1a**. Figure generated using ORTEP-3.(Farrugia, 2012)

Table S1. Selected hydrogen-bond parameters

D—H···*A*	*D*—H (Å)	H···*A* (Å)	*D*···*A* (Å)	*D*—H···*A* (°)
C38—H38A···I2A[a]i	0.97	3.33	4.098 (15)	137.9
C42—H42A···I2Aa[ii]	0.97	3.28	3.948 (14)	127.4

Symmetry code(s): (i) -*x*, -*y*+1, -*z*+1; (ii) -*x*+1, -*y*+1, -*z*+1.

Table S2. Selected geometric parameters (Å, º)

I1—C1	2.167 (16)	C26—C27	1.39 (2)
F1—C1	1.303 (19)	C26—H26	0.9300
F2—C1	1.385 (19)	C27—C28	1.37 (2)
F3—C2	1.329 (14)	C27—H27	0.9300
F4—C2	1.324 (14)	C28—C29	1.40 (2)
F5—C3	1.373 (15)	C28—H28	0.9300
F6—C3	1.324 (15)	C29—C30	1.39 (2)
C1—C2	1.487 (19)	C29—H29	0.9300
C2—C3	1.536 (17)	C30—H30	0.9300
C3—C3^{i}	1.51 (3)	C31—C36	1.506 (19)
P1—C13	1.832 (15)	C31—C32	1.52 (2)
P1—C19	1.848 (15)	C31—H31	0.9800
P1—C7	1.863 (16)	C32—C33	1.50 (2)
P2—C25	1.802 (15)	C32—H32A	0.9700
P2—C37	1.847 (15)	C32—H32B	0.9700
P2—C31	1.852 (16)	C33—C34	1.47 (2)
C7—C8	1.37 (2)	C33—H33A	0.9700
C7—C12	1.39 (2)	C33—H33B	0.9700
C8—C9	1.38 (2)	C34—C35	1.46 (2)
C8—H8	0.9300	C34—H34A	0.9700
C9—C10	1.37 (2)	C34—H34B	0.9700
C9—H9	0.9300	C35—C36	1.50 (2)
C10—C11	1.35 (2)	C35—H35A	0.9700
C10—H10	0.9300	C35—H35B	0.9700
C11—C12	1.37 (2)	C36—H36A	0.9700
C11—H11	0.9300	C36—H36B	0.9700
C12—H12	0.9300	C37—C42	1.521 (18)
C13—C18	1.510 (19)	C37—C38	1.523 (19)
C13—C14	1.545 (19)	C37—H37	0.9800
C13—H13	0.9800	C38—C39	1.526 (19)

C14—C15	1.53 (2)	C38—H38A	0.9700
C14—H14A	0.9700	C38—H38B	0.9700
C14—H14B	0.9700	C39—C40	1.517 (19)
C15—C16	1.52 (2)	C39—H39A	0.9700
C15—H15A	0.9700	C39—H39B	0.9700
C15—H15B	0.9700	C40—C41	1.51 (2)
C16—C17	1.52 (2)	C40—H40A	0.9700
C16—H16A	0.9700	C40—H40B	0.9700
C16—H16B	0.9700	C41—C42	1.507 (19)
C17—C18	1.52 (2)	C41—H41A	0.9700
C17—H17A	0.9700	C41—H41B	0.9700
C17—H17B	0.9700	C42—H42A	0.9700
C18—H18A	0.9700	C42—H42B	0.9700
C18—H18B	0.9700	I2A—C4A	2.17 (2)
C19—C24	1.512 (19)	F7A—C4A	1.32 (2)
C19—C20	1.54 (2)	F8A—C4A	1.39 (2)
C19—H19	0.9800	F9A—C5A	1.337 (19)
C20—C21	1.53 (2)	F10A—C5A	1.343 (18)
C20—H20A	0.9700	F11A—C6A	1.38 (2)
C20—H20B	0.9700	F12A—C6A	1.31 (2)
C21—C22	1.49 (2)	C4A—C5A	1.49 (2)
C21—H21A	0.9700	C5A—C6A	1.54 (2)
C21—H21B	0.9700	C6A—C6A^{ii}	1.62 (5)
C22—C23	1.50 (2)	I2B—C4B	2.180 (19)
C22—H22A	0.9700	F7B—C4B	1.31 (2)
C22—H22B	0.9700	F8B—C4B	1.40 (2)
C23—C24	1.54 (2)	F9B—C5B	1.338 (19)
C23—H23A	0.9700	F10B—C5B	1.342 (18)
C23—H23B	0.9700	F11B—C6B	1.40 (2)
C24—H24A	0.9700	F12B—C6B	1.31 (2)
C24—H24B	0.9700	C4B—C5B	1.49 (2)

C25—C30	1.38 (2)	C5B—C6B	1.54 (2)
C25—C26	1.40 (2)	C6B—C6B^{ii}	1.39 (5)
F1—C1—F2	104.7 (15)	C28—C27—C26	121.7 (18)
F1—C1—C2	110.0 (15)	C28—C27—H27	119.1
F2—C1—C2	105.5 (14)	C26—C27—H27	119.1
F1—C1—I1	112.0 (12)	C27—C28—C29	118.1 (17)
F2—C1—I1	106.9 (11)	C27—C28—H28	121.0
C2—C1—I1	116.8 (11)	C29—C28—H28	121.0
F4—C2—F3	107.0 (12)	C30—C29—C28	119.5 (17)
F4—C2—C1	106.5 (13)	C30—C29—H29	120.2
F3—C2—C1	104.9 (13)	C28—C29—H29	120.2
F4—C2—C3	108.6 (11)	C25—C30—C29	122.2 (16)
F3—C2—C3	109.1 (11)	C25—C30—H30	118.9
C1—C2—C3	119.9 (12)	C29—C30—H30	118.9
F6—C3—F5	107.5 (11)	C36—C31—C32	112.8 (13)
F6—C3—C3^{i}	112.2 (16)	C36—C31—P2	119.0 (11)
F5—C3—C3^{i}	106.2 (15)	C32—C31—P2	112.1 (11)
F6—C3—C2	108.5 (12)	C36—C31—H31	103.6
F5—C3—C2	105.9 (11)	C32—C31—H31	103.6
C3^{i}—C3—C2	115.9 (15)	P2—C31—H31	103.6
C13—P1—C19	104.4 (7)	C33—C32—C31	113.0 (14)
C13—P1—C7	104.3 (7)	C33—C32—H32A	109.0
C19—P1—C7	104.4 (7)	C31—C32—H32A	109.0
C25—P2—C37	104.2 (7)	C33—C32—H32B	109.0
C25—P2—C31	102.9 (8)	C31—C32—H32B	109.0
C37—P2—C31	105.7 (7)	H32A—C32—H32B	107.8
C8—C7—C12	119.8 (15)	C34—C33—C32	115.4 (16)
C8—C7—P1	116.6 (13)	C34—C33—H33A	108.4
C12—C7—P1	123.5 (14)	C32—C33—H33A	108.4
C7—C8—C9	119.4 (16)	C34—C33—H33B	108.4
C7—C8—H8	120.3	C32—C33—H33B	108.4

C9—C8—H8	120.3	H33A—C33—H33B	107.5
C10—C9—C8	120.2 (17)	C35—C34—C33	112.3 (16)
C10—C9—H9	119.9	C35—C34—H34A	109.1
C8—C9—H9	119.9	C33—C34—H34A	109.1
C11—C10—C9	120.7 (17)	C35—C34—H34B	109.1
C11—C10—H10	119.7	C33—C34—H34B	109.1
C9—C10—H10	119.7	H34A—C34—H34B	107.9
C10—C11—C12	120.1 (18)	C34—C35—C36	114.1 (15)
C10—C11—H11	119.9	C34—C35—H35A	108.7
C12—C11—H11	119.9	C36—C35—H35A	108.7
C11—C12—C7	119.8 (17)	C34—C35—H35B	108.7
C11—C12—H12	120.1	C36—C35—H35B	108.7
C7—C12—H12	120.1	H35A—C35—H35B	107.6
C18—C13—C14	108.6 (13)	C35—C36—C31	112.3 (13)
C18—C13—P1	112.0 (10)	C35—C36—H36A	109.1
C14—C13—P1	110.6 (10)	C31—C36—H36A	109.1
C18—C13—H13	108.5	C35—C36—H36B	109.1
C14—C13—H13	108.5	C31—C36—H36B	109.1
P1—C13—H13	108.5	H36A—C36—H36B	107.9
C15—C14—C13	112.7 (13)	C42—C37—C38	109.5 (12)
C15—C14—H14A	109.1	C42—C37—P2	110.7 (10)
C13—C14—H14A	109.1	C38—C37—P2	110.8 (10)
C15—C14—H14B	109.1	C42—C37—H37	108.6
C13—C14—H14B	109.1	C38—C37—H37	108.6
H14A—C14—H14B	107.8	P2—C37—H37	108.6
C16—C15—C14	110.5 (14)	C37—C38—C39	111.6 (12)
C16—C15—H15A	109.5	C37—C38—H38A	109.3
C14—C15—H15A	109.5	C39—C38—H38A	109.3
C16—C15—H15B	109.5	C37—C38—H38B	109.3
C14—C15—H15B	109.5	C39—C38—H38B	109.3
H15A—C15—H15B	108.1	H38A—C38—H38B	108.0

C17—C16—C15	110.3 (14)	C40—C39—C38	110.6 (12)
C17—C16—H16A	109.6	C40—C39—H39A	109.5
C15—C16—H16A	109.6	C38—C39—H39A	109.5
C17—C16—H16B	109.6	C40—C39—H39B	109.5
C15—C16—H16B	109.6	C38—C39—H39B	109.5
H16A—C16—H16B	108.1	H39A—C39—H39B	108.1
C18—C17—C16	110.5 (14)	C41—C40—C39	113.0 (13)
C18—C17—H17A	109.5	C41—C40—H40A	109.0
C16—C17—H17A	109.5	C39—C40—H40A	109.0
C18—C17—H17B	109.5	C41—C40—H40B	109.0
C16—C17—H17B	109.5	C39—C40—H40B	109.0
H17A—C17—H17B	108.1	H40A—C40—H40B	107.8
C13—C18—C17	113.4 (14)	C42—C41—C40	111.0 (13)
C13—C18—H18A	108.9	C42—C41—H41A	109.4
C17—C18—H18A	108.9	C40—C41—H41A	109.4
C13—C18—H18B	108.9	C42—C41—H41B	109.4
C17—C18—H18B	108.9	C40—C41—H41B	109.4
H18A—C18—H18B	107.7	H41A—C41—H41B	108.0
C24—C19—C20	107.9 (13)	C41—C42—C37	113.1 (13)
C24—C19—P1	115.3 (11)	C41—C42—H42A	109.0
C20—C19—P1	110.7 (10)	C37—C42—H42A	109.0
C24—C19—H19	107.5	C41—C42—H42B	109.0
C20—C19—H19	107.5	C37—C42—H42B	109.0
P1—C19—H19	107.5	H42A—C42—H42B	107.8
C21—C20—C19	112.8 (14)	F7A—C4A—F8A	109.3 (16)
C21—C20—H20A	109.0	F7A—C4A—C5A	110 (2)
C19—C20—H20A	109.0	F8A—C4A—C5A	105 (2)
C21—C20—H20B	109.0	F7A—C4A—I2A	110.1 (18)
C19—C20—H20B	109.0	F8A—C4A—I2A	106.5 (17)
H20A—C20—H20B	107.8	C5A—C4A—I2A	115.0 (14)
C22—C21—C20	111.8 (16)	F9A—C5A—F10A	111.0 (15)

C22—C21—H21A	109.3	F9A—C5A—C4A	103.1 (18)
C20—C21—H21A	109.3	F10A—C5A—C4A	108.8 (19)
C22—C21—H21B	109.3	F9A—C5A—C6A	109.3 (18)
C20—C21—H21B	109.3	F10A—C5A—C6A	106.0 (17)
H21A—C21—H21B	107.9	C4A—C5A—C6A	118.7 (17)
C21—C22—C23	111.8 (15)	F12A—C6A—F11A	110.2 (16)
C21—C22—H22A	109.2	F12A—C6A—C5A	109.2 (19)
C23—C22—H22A	109.2	F11A—C6A—C5A	104.0 (19)
C21—C22—H22B	109.2	F12A—C6A—C6A^{ii}	113 (3)
C23—C22—H22B	109.2	F11A—C6A—C6A^{ii}	103 (2)
H22A—C22—H22B	107.9	C5A—C6A—C6A^{ii}	117 (2)
C22—C23—C24	111.4 (15)	F7B—C4B—F8B	109.0 (15)
C22—C23—H23A	109.3	F7B—C4B—C5B	108.4 (18)
C24—C23—H23A	109.3	F8B—C4B—C5B	102.9 (18)
C22—C23—H23B	109.3	F7B—C4B—I2B	112.7 (15)
C24—C23—H23B	109.3	F8B—C4B—I2B	105.4 (17)
H23A—C23—H23B	108.0	C5B—C4B—I2B	117.7 (14)
C19—C24—C23	112.4 (14)	F9B—C5B—F10B	111.0 (15)
C19—C24—H24A	109.1	F9B—C5B—C4B	104.7 (18)
C23—C24—H24A	109.1	F10B—C5B—C4B	106.9 (17)
C19—C24—H24B	109.1	F9B—C5B—C6B	106.4 (17)
C23—C24—H24B	109.1	F10B—C5B—C6B	108.7 (17)
H24A—C24—H24B	107.8	C4B—C5B—C6B	119.1 (16)
C30—C25—C26	117.1 (14)	F12B—C6B—C6B^{ii}	112 (3)
C30—C25—P2	117.7 (12)	F12B—C6B—F11B	108.9 (15)
C26—C25—P2	124.9 (12)	C6B^{ii}—C6B—F11B	97 (3)
C27—C26—C25	120.2 (16)	F12B—C6B—C5B	112 (2)
C27—C26—H26	119.9	C6B^{ii}—C6B—C5B	122 (2)
C25—C26—H26	119.9	F11B—C6B—C5B	104.3 (18)
F1—C1—C2—F4	−171.4 (15)	C26—C25—C30—C29	−8 (3)
F2—C1—C2—F4	−59.0 (17)	P2—C25—C30—C29	178.5 (13)

I1—C1—C2—F4	59.5 (16)	C28—C29—C30—C25	8 (3)
F1—C1—C2—F3	75.4 (17)	C25—P2—C31—C36	68.1 (14)
F2—C1—C2—F3	−172.2 (13)	C37—P2—C31—C36	−40.9 (14)
I1—C1—C2—F3	−53.7 (16)	C25—P2—C31—C32	−66.6 (13)
F1—C1—C2—C3	−48 (2)	C37—P2—C31—C32	−175.6 (11)
F2—C1—C2—C3	64.7 (19)	C36—C31—C32—C33	45 (2)
I1—C1—C2—C3	−176.7 (11)	P2—C31—C32—C33	−177.0 (12)
F4—C2—C3—F6	73.5 (14)	C31—C32—C33—C34	−46 (2)
F3—C2—C3—F6	−170.2 (12)	C32—C33—C34—C35	49 (2)
C1—C2—C3—F6	−49.3 (19)	C33—C34—C35—C36	−52 (2)
F4—C2—C3—F5	−171.3 (12)	C34—C35—C36—C31	52 (2)
F3—C2—C3—F5	−55.0 (14)	C32—C31—C36—C35	−48.4 (19)
C1—C2—C3—F5	66.0 (18)	P2—C31—C36—C35	177.2 (12)
F4—C2—C3—C3^{i}	−54 (2)	C25—P2—C37—C42	63.7 (12)
F3—C2—C3—C3^{i}	62 (2)	C31—P2—C37—C42	171.7 (10)
C1—C2—C3—C3^{i}	−176.6 (17)	C25—P2—C37—C38	−174.6 (11)
C13—P1—C7—C8	146.8 (12)	C31—P2—C37—C38	−66.5 (12)
C19—P1—C7—C8	−103.9 (13)	C42—C37—C38—C39	−56.2 (16)
C13—P1—C7—C12	−36.7 (15)	P2—C37—C38—C39	−178.6 (10)
C19—P1—C7—C12	72.5 (14)	C37—C38—C39—C40	55.6 (17)
C12—C7—C8—C9	2 (2)	C38—C39—C40—C41	−53.7 (18)
P1—C7—C8—C9	178.3 (12)	C39—C40—C41—C42	52.7 (18)
C7—C8—C9—C10	−3 (3)	C40—C41—C42—C37	−54.0 (18)
C8—C9—C10—C11	3 (3)	C38—C37—C42—C41	55.7 (17)
C9—C10—C11—C12	−1 (3)	P2—C37—C42—C41	178.2 (11)
C10—C11—C12—C7	0 (3)	F7A—C4A—C5A—F9A	63 (2)
C8—C7—C12—C11	0 (2)	F8A—C4A—C5A—F9A	−178.8 (19)
P1—C7—C12—C11	−176.3 (12)	I2A—C4A—C5A—F9A	−62 (2)
C19—P1—C13—C18	61.0 (13)	F7A—C4A—C5A—F10A	−179 (2)
C7—P1—C13—C18	170.3 (11)	F8A—C4A—C5A—F10A	−61 (2)
C19—P1—C13—C14	−177.7 (11)	I2A—C4A—C5A—F10A	56 (2)

C7—P1—C13—C14	−68.5 (12)	F7A—C4A—C5A—C6A	−58 (3)
C18—C13—C14—C15	−54.1 (19)	F8A—C4A—C5A—C6A	60 (3)
P1—C13—C14—C15	−177.3 (12)	I2A—C4A—C5A—C6A	177.0 (16)
C13—C14—C15—C16	56 (2)	F9A—C5A—C6A—F12A	−172 (2)
C14—C15—C16—C17	−57 (2)	F10A—C5A—C6A—F12A	68 (2)
C15—C16—C17—C18	57 (2)	C4A—C5A—C6A—F12A	−54 (3)
C14—C13—C18—C17	54.8 (19)	F9A—C5A—C6A—F11A	−54 (2)
P1—C13—C18—C17	177.2 (12)	F10A—C5A—C6A—F11A	−174 (2)
C16—C17—C18—C13	−58 (2)	C4A—C5A—C6A—F11A	63 (3)
C13—P1—C19—C24	135.8 (12)	F9A—C5A—C6A—C6A^{ii}	58 (3)
C7—P1—C19—C24	26.7 (14)	F10A—C5A—C6A—C6A^{ii}	−61 (3)
C13—P1—C19—C20	−101.3 (12)	C4A—C5A—C6A—C6A^{ii}	176 (2)
C7—P1—C19—C20	149.5 (12)	F7B—C4B—C5B—F9B	68 (2)
C24—C19—C20—C21	−55.1 (19)	F8B—C4B—C5B—F9B	−177.0 (17)
P1—C19—C20—C21	177.9 (13)	I2B—C4B—C5B—F9B	−62 (2)
C19—C20—C21—C22	55 (2)	F7B—C4B—C5B—F10B	−174.6 (18)
C20—C21—C22—C23	−54 (2)	F8B—C4B—C5B—F10B	−59 (2)
C21—C22—C23—C24	54 (2)	I2B—C4B—C5B—F10B	56 (2)
C20—C19—C24—C23	55.5 (18)	F7B—C4B—C5B—C6B	−51 (3)
P1—C19—C24—C23	179.8 (12)	F8B—C4B—C5B—C6B	64 (2)
C22—C23—C24—C19	−56 (2)	I2B—C4B—C5B—C6B	179.5 (15)
C37—P2—C25—C30	−148.6 (13)	F9B—C5B—C6B—F12B	−162 (2)
C31—P2—C25—C30	101.2 (14)	F10B—C5B—C6B—F12B	78 (2)
C37—P2—C25—C26	38.4 (16)	C4B—C5B—C6B—F12B	−44 (3)
C31—P2—C25—C26	−71.8 (16)	F9B—C5B—C6B—C6B^{ii}	63 (3)
C30—C25—C26—C27	8 (2)	F10B—C5B—C6B—C6B^{ii}	−57 (3)
P2—C25—C26—C27	−178.5 (13)	C4B—C5B—C6B—C6B^{ii}	−179 (3)
C25—C26—C27—C28	−10 (3)	F9B—C5B—C6B—F11B	−44 (2)
C26—C27—C28—C29	10 (3)	F10B—C5B—C6B—F11B	−164 (2)
C27—C28—C29—C30	−9 (3)	C4B—C5B—C6B—F11B	73 (3)

Symmetry code(s): (i) −*x*+2, −*y*, −*z*+1; (ii) −*x*+1, −*y*, −*z*+1.

References

Aakeröy, C. B., Wijethunga, T. K., Desper, J. & Đaković, M. (2015). *Cryst. Growth Des.* **15**, 3853-3861.

Abate, A., Biella, S., Cavallo, G., Meyer, F., Neukirch, H., Metrangolo, P., Pilati, T., Resnati, G. & Terraneo, G. (2009). *J. Fluorine Chem.* **130**, 1171-1177.

Anderson, B. J., Guino-o, M. A., Glueck, D. S., Golen, J. A., DiPasquale, A. G., Liable-Sands, L. M. & Rheingold, A. L. (2008). *Org. Lett.* **10**, 4425-4428.

Berger, G., Soubhye, J. & Meyer, F. (2015). *Polym. Chem.* **6**, 3559-3580.

Blessing, R. H. (1995). *Acta Crystallogr. A* **51 (Pt 1)**, 33-38.

Braga, D., Maini, L. & Grepioni, F. (2013). *Chem. Soc. Rev.* **42**, 7638-7648.

Brown, A. & Beer, P. D. (2016). *Chem. Commun.* **52**, 8645-8658.

Bruker (2010). *APEX Suite.* Madison, Wisconsin, USA.

Bryce, D. L., Bernard, G. M., Gee, M., Lumsden, M. D., Eichele, K. & Wasylishen, R. E. (2001) *Can. J. Anal. Sci. Spectrosc.* **46**, 46-82.

Bryce, D. L. & Taulelle, F. (2017) *Acta Cryst. C* **73**, 126-127.

Bulfield, D. & Huber, S. M. (2016). *Chem. Eur. J.* **22**, 14434-14450.

Carstens, T., Haynes, D. A. & Smith, V. J. (2019). *Cryst. Growth Des.* **20**, 1139-1149.

Catalano, L., Perez-Estrada, S., Terraneo, G., Pilati, T., Resnati, G., Metrangolo, P. & Garcia-Garibay, M. A. (2015). *J. Am. Chem. Soc.* **137**, 15386-15389.

Catalano, L., Perez-Estrada, S., Wang, H. H., Ayitou, A. J., Khan, S. I., Terraneo, G., Metrangolo, P., Brown, S. & Garcia-Garibay, M. A. (2017). *J. Am. Chem. Soc.* **139**, 843-848.

Cavallo, G., Metrangolo, P., Milani, R., Pilati, T., Priimagi, A., Resnati, G. & Terraneo, G. (2016). *Chem. Rev.* **116**, 2478-2601.

Cerreia Vioglio, P., Catalano, L., Vasylyeva, V., Nervi, C., Chierotti, M. R., Resnati, G., Gobetto, R. & Metrangolo, P. (2016). *Chem. Eur. J.* **22**, 16819-16828.

Cerreia Vioglio, P., Szell, P. M. J., Chierotti, M. R., Gobetto, R. & Bryce, D. L. (2018). *Chem. Sci.* **9**, 4555-4561.

Christopherson, J. C., Topić, F., Barrett, C. J. & Friščić, T. (2018). *Cryst. Growth Des.* **18**, 1245-1259.

Cinčić, D., Friščić, T. & Jones, W. (2008a). *Chem. Eur. J.* **14**, 747-753.

Cinčić, D., Friščić, T. & Jones, W. (2008b). *J. Am. Chem. Soc.* **130**, 7524-7525.

Clark, T., Hennemann, M., Murray, J. S. & Politzer, P. (2007). *J. Mol. Model.* **13**, 291-296.

Decato, D. A., Riel, A. M. S., May, J. H., Bryantsev, V. S. & Berryman, O. B. (2020). *Angew. Chem.* **133**, 3729-3736.

Engel, E. A., Anelli, A., Hofstetter, A., Paruzzo, F., Emsley, L. & Ceriotti, M. (2019) *Phys. Chem. Chem. Phys.* **21**, 23385-23400.

Eraković, M., Nemec, V., Lež, T., Porupski, I., Stilinović, V. & Cinčić, D. (2018). *Cryst. Growth Des.* **18**, 1182-1190.

Farrugia, L. J. (2012). *J. Appl. Crystallogr.* **45**, 849-854.

Fischer, F., Lubjuhn, D., Greiser, S., Rademann, K. & Emmerling, F. (2016). *Cryst. Growth Des.* **16**, 5843-5851.

Fung, B. M., Khitrin, A. K. & Ermolaev, K. (2000). *J. Magn. Reson.* **142**, 97-101.

Gao, H. Y., Shen, Q. J., Zhao, X. R., Yan, X. Q., Pang, X. & Jin, W. J. (2012). *J. Mater. Chem.* **22**.

Garabadzhiu, A. V., Kuznetsov, V. A., Maslennikov, I. G., Lavrent'ev, A. N. & Sochilin, E. G. (1980). *Zh. Obshch. Khim.* **50**, 1463-1467.

Garabadzhiu, A. V., Kuznetsov, V. A., Shibaev, V. I., Lavrentev, A. N. & Sochilin, E. G. (1979). *Zh. Obshch. Khim.* **49**, 2223-2225.

Garabadzhiu, A. V., Shibaev, V. I., Lavrent'ev, A. N. & Sochilin, E. G. (1979). *Zh. Obshch. Khim.* **49**, 1501-1503.

Gilday, L. C., Robinson, S. W., Barendt, T. A., Langton, M. J., Mullaney, B. R. & Beer, P. D. (2015). *Chem. Rev.* **115**, 7118-7195.

Groom, C. R., Bruno, I. J., Lightfoot, M. P. & Ward, S. C. (2016). *Acta Crystallogr. Sect. B: Struct. Sci.* **72**, 171-179.

Harris, R. K., Wasylishen, R. E. & Duer, M. J., Eds. *NMR Crystallography*. Wiley, Chichester, 2009.

Hodgkinson, P. (2020) *Prog. Nucl. Magn. Reson. Spectrosc.* **118-119**, 10-53.

Hubschle, C. B., Sheldrick, G. M. & Dittrich, B. (2011). *J. Appl. Crystallogr.* **44**, 1281-1284.

Jungbauer, S. H. & Huber, S. M. (2015). *J. Am. Chem. Soc.* **137**, 12110-12120.

King, H. W. & Payzant, E. A. (2001) *Can. Metallurg. Quarterly* **40**, 385-394.

Langton, M. J., Robinson, S. W., Marques, I., Felix, V. & Beer, P. D. (2014). *Nat. Chem.* **6**, 1039-1043.

Lemouchi, C., Vogelsberg, C. S., Zorina, L., Simonov, S., Batail, P., Brown, S. & Garcia-Garibay, M. A. (2011). *J. Am. Chem. Soc.* **133**, 6371-6379.

Li, B., Zang, S.-Q., Wang, L.-Y. & Mak, T. C. W. (2016). *Coord. Chem. Rev.* **308**, 1-21.

Lisac, K., Nemec, V., Topić, F., Arhangelskis, M., Hindle, P., Tran, R., Huskić, I., Morris, A. J., Friščić, T. & Cinčić, D. (2018). *Cryst. Growth Des.* **18**, 2387-2396.

Lisac, K., Topic, F., Arhangelskis, M., Cepic, S., Julien, P. A., Nickels, C. W., Morris, A. J., Friščić, T. & Cinčić, D. (2019). *Nat. Commun.* **10**, 61.

Martineau, C., Senker, J. & Taulelle, F. (2014) *Annu. Rep. Nucl. Magn. Reson. Spectrosc.* **82**, 1-57.

Metrangolo, P., Neukirch, H., Pilati, T. & Resnati, G. (2005). *Acc. Chem. Res.* **38**, 386-395.

Metz, G., Wu, X. L. & Smith, S. O. (1994). *J. Magn. Reson., Ser A* **110**, 219-227.

Morin, V. M., Szell, P. M. J., Caron-Poulin, E., Gabidullin, B. & Bryce, D. L. (2019). *ChemistryOpen* **8**, 1328-1336.

Pérez-Torralba, M., García, M. Á., López, C., Torralba, M. C., Torres, M. R., Claramunt, R. M. & Elguero, J. (2014). *Cryst. Growth Des.* **14**, 3499-3509.

Priimagi, A., Cavallo, G., Metrangolo, P. & Resnati, G. (2013). *Acc. Chem. Res.* **46**, 2686-2695.

Riley, K. E., Murray, J. S., Fanfrlik, J., Rezac, J., Sola, R. J., Concha, M. C., Ramos, F. M. & Politzer, P. (2011). *J. Mol. Model.* **17**, 3309-3318.

Riley, K. E., Murray, J. S., Fanfrlik, J., Rezac, J., Sola, R. J., Concha, M. C., Ramos, F. M. & Politzer, P. (2013). *J. Mol. Model.* **19**, 4651-4659.

Sheldrick, G. M. (2008). *Acta Crystallogr. A* **64**, 112-122.

Siegfried, A. M., Arman, H. D., Kobra, K., Liu, K., Peloquin, A. J., McMillen, C. D., Hanks, T. & Pennington, W. T. (2020). *Cryst. Growth Des.* **20**, 7460-7469.

Szell, P. M. J. & Bryce, D. L. (2016). *J. Phys. Chem. C* **120**, 11121-11130.

Szell, P. M. J., Cavallo, G., Terraneo, G., Metrangolo, P., Gabidullin, B. & Bryce, D. L. (2018). *Chem. Eur. J.* **24**, 11364-11376.

Szell, P. M. J., Dragon, J., Zablotny, S., Harrigan, S. R., Gabidullin, B. & Bryce, D. L. (2018). *New J. Chem.* **42**, 10493-10501.

Szell, P. M. J., Gabriel, S. A., Caron-Poulin, E., Jeannin, O., Fourmigué, M. & Bryce, D. L. (2018). *Cryst. Growth Des.* **18**, 6227-6238.

Szell, P. M. J., Grebert, L. & Bryce, D. L. (2019). *Angew. Chem. Int. Ed. Engl.* **58**, 13479-13485.

Szell, P. M. J., Zablotny, S. & Bryce, D. L. (2019). *Nat. Commun.* **10**, 916.

Tepper, R. & Schubert, U. S. (2018). *Angew. Chem. Int. Ed. Engl.* **57**, 6004-6016.

Terskikh, V. V., Lang, S. J., Gordon, P. G., Enright, G. D. & Ripmeester, J. A. (2009). *Magn. Reson. Chem.* **47**, 398-406.

Tusy, C., Huang, L., Jin, J. & Xia, J. (2014) *RSC Adv.***4**, 8011-8014.

Ungár, T. (2001) *Mat. Sci. Eng. A* **309-310**, 14-22.

Ungati, H., Govindaraj, V. & Mugesh, G. (2018). *Angew. Chem. Int. Ed. Engl.* **57**, 8989-8993.

Viger-Gravel, J., Korobkov, I. & Bryce, D. L. (2011). *Cryst. Growth Des.* **11**, 4984-4995.

Viger-Gravel, J., Leclerc, S., Korobkov, I. & Bryce, D. L. (2013). *CrystEngComm* **15**, 3168-3177.

Viger-Gravel, J., Leclerc, S., Korobkov, I. & Bryce, D. L. (2014). *J. Am. Chem. Soc.* **136**, 6929-6942.

Viger-Gravel, J., Meyer, J. E., Korobkov, I. & Bryce, D. L. (2014). *CrystEngComm* **16**, 7285-7297.

Vioglio, P. C., Chierotti, M. R. & Gobetto, R. (2016). *CrystEngComm* **18**, 9173-9184.

Weingarth, M., Raouafi, N., Jouvelet, B., Duma, L., Bodenhausen, G., Boujlel, K., Schollhorn, B. & Tekely, P. (2008). *Chem. Commun.* 5981-5983.

Xu, Y., Southern, S. A., Szell, P. M. J. & Bryce, D. L. (2016) *CrystEngComm* **18**, 5236-5252.

Xu, Y., Huang, J., Gabidullin, B. & Bryce, D. L. (2018). *Chem. Commun.* **54**, 11041-11043.

Xu, Y., Szell, P. M. J., Kumar, V. & Bryce, D. L. (2020). *Coord. Chem. Rev.* **411**, 213237.

Xu, Y., Viger-Gravel, J., Korobkov, I. & Bryce, D. L. (2015). *J. Phys. Chem. C* **119**, 27104-27117.

Chapter 4 – Valence p-Orbital Population Anisotropy in Halogen-Bonded Systems

4.1 - Objectives

The following section focuses on the different theoretical concepts necessary to the proper comprehension of this project, including the results, discussion and conclusion of this report. The main objective of this project is to understand and correlate the use of a newly reported parameter,[34] VPPA, valence p-orbital population anisotropy, with the origins of the electric field gradients (EFG) in halogen-bonded systems. To do so, computational work on models and real halogen-bonded crystal systems will be done using standard hybrid density functional theory (DFT) methods. P-orbital populations will be generated and used to compute the VPPA. The utility of the VPPA parameter, linked with the EFG, will be discussed as a tool to assess particular donors' ability to engage in halogen bonds.

4.2 – Townes-Dailey Model

This model involves the field gradients generated by the *p* electrons and is usually used to estimate the fraction of ionic character from a single nuclear quadrupolar coupling constant of diatomic molecules. The TD model asserts that only the *p* electrons of the atom need to be taken into consideration since the core electrons consist of filled shells and are spherically symmetrical. The *s* electrons produce zero field gradient and *d* electrons do produce a field gradient but since it has been estimated to be smaller than the *p* electrons by a factor of 47, it can be neglected.[35] In relation with NQR, one of the most widely used approaches to provide a meaningful account of bonding trends within a series of related compounds is that formulated by Townes and Dailey for the interpretation of nuclear quadrupole interactions (NQI). [23] The

electric field gradient at a quadrupolar nucleus is influenced mainly from electrons of the same atom. As a first approximation, the internal electron distribution may be considered spherically symmetric due to its closed environment. Therefore, they will not contribute to the EFG. If the only purpose for the NQI comparison is chemical interpretation and not discussion of their absolute meanings, then the polarization of the internal electrons can be neglected. For the valence electrons, *s*-orbital ones that are spherically symmetric do not contribute to the EFG and their main contribution is caused by *p*-electrons; because of the more significant distance from the nucleus and their smaller participation in hybridization, d and f electrons' contribution to the EFG is much less. In a recent paper by Wu and Rinald,[34] a modified Townes-Dailey (TD) model was proposed to help interpret and visualize nuclear quadrupolar coupling tensors (NQCT) and EFGs in organic molecules. It is shown that each principal component of the NQCT is directly related to a new quantity, the valence p-orbital population anisotropy (VPPA or ΔP) within the TD model framework. This proposed model is actually a simple reformulation of the original TD model and does not introduce new concepts, but this new proposition makes it possible to directly visualize and interpret more straightforwardly the experimentally determined NQCTs in different molecules. The utilization of VPPA for different nuclei such as ^{11}B, ^{14}N, ^{17}O, ^{35}Cl, ^{79}Br, and ^{127}I were done and compared.

In this project, we applied the new VPPA knowledge to our groups' previously reported extensive experimental NMR and NQR data relating ^{35}Cl, ^{79}Br, and ^{127}I nuclei quadrupolar coupling information to local molecular structure in halogen-bonded systems.[36] VPPA will be used to increase the understanding of the origins of the EFGs in halogen-bonded systems.

4.3 – VPPA Parameter

Valence p-orbital population anisotropy (VPPA or ΔP) describes the p-orbital population imbalance in each of the 3 principal-axis directions for each valence p-orbital wave function.

$$\Delta P_{ii} = P_{ii} - P_{ave}$$

Where $P_{ave} = \frac{1}{3}(P_{ii} + P_{jj} + P_{kk})$

Equation 10. Valence p-orbital population anisotropy (VPPA or ΔP)

A positive ΔP_{ii} in one direction means that the p-orbital population is in excess (of electrons) in that direction whereas a negative ΔP_{ii} means that the p-orbital population is deficient. Some advantages of using VPPA ellipsoids to represent quadrupolar coupling tensors are that it has a clear physical meaning and can often be linked directly to the Lewis structure of the molecule of interest. If the ΔP_{ii} is very positive (high value), it is usually related to the direction of electron lone pairs. If ΔP_{ii} is very negative, it can be linked to the presence of σ-holes. On the basis of ΔP_{zz} and the equations below, it is easier to understand the sign of C_Q, the quadrupolar coupling constant.

The quadrupolar tensor component χ_0 is defined as the contribution from a single electron residing in the p_z orbital to the z-component of the quadrupolar coupling (QC) tensor. As represented in Figure 23 the x and y components of the QC tensor (axially symmetric) are of the same value (- $\chi_0/2$) since the QC tensor must be traceless. The sign of χ_0 can be positive or negative, it depends on the sign of Q; The sign of χ_0 will always be the opposite of that of Q.

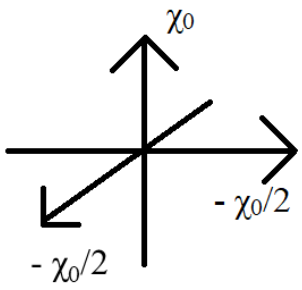

Figure 23: Sign of χ_0

4.4 – Computational methods

All computational calculations were carried out using the Gaussian 09 software[37] on the UOttawa Wooki Cluster.[38] The model compounds were constructed and visualized via GaussView 4.1 software for Microsoft Windows.[39] All CIF files were viewed and edited on Mercury and then visualized using GaussView 4.1 software.

All calculations were conducted with the 6-311G(3df) basis set except for ^{127}I and ^{79}Br molecules, where the DGDZVP basis set was used (more preferable with heavy atoms). The compounds (O test molecules are shown in Table 4, Br molecules are shown in Table 5 and Figure 27 and I molecules are shown in Table 7 and Figure 31) were first geometry optimized on the hydrogen atoms using DFT (B3LYP level of theory) methods with keywords geom=connectivity. A population and NBO analysis was also implemented with keywords "pop=(nbo, savenbo)". Direct calculations of EFG tensors were then performed using the "prop" keyword. *P*-orbital information and EFG tensor components were taken from the output file under NBO analysis and the electrostatic properties using SCF density section respectively. EFGShield version 4.6[40] was used to extract the calculated C_Q.

4.5 – Results and Discussion

Initially, trial test runs were performed first to ensure reproducible and consistent results with the literature as well as to become familiar with the Gaussian program and calculations. This was done using ^{17}O as the nucleus of interest. The molecules created in Gaussview and used in calculations were formaldehyde, ethylene oxide, dimethyl ether, water, carbon monoxide, furan and hypofluorite (see Table 4). As a theory reminder for calculating χ_{ii} , the three principal components of the quadrupole coupling (QC) tensor

$$\chi_{ii} = {}^{3}/_{2} \cdot \chi_0 \cdot \Delta P_{ii}$$

Equation 11: Modified Townes-Dailey calculated χ_{ii}

$$\chi_{ii} = 2.349 \cdot Q \cdot V_{ii}$$

Equation 12: Direct calculation of χ_{ii}

EFG tensor components can be found under the *Electrostatic Properties Using the SCF Density* section in the output file. An example with formaldehyde is shown in Figure 24 and Figure 25 below.

Center	---- Electric Field Gradient ---- (tensor representation) ---- Eigenvalues ----		
1 Atom	-0.451398	0.136314	0.315084
2 Atom	-1.709352	-0.586719	2.296072
3 Atom	-0.285924	0.142236	0.143688
4 Atom	-0.285924	0.142236	0.143688

Figure 24: Formaldehyde's V_{ii} Electric field gradient tensor components under the Electrostatic Properties using the SCF Density section in the output file.

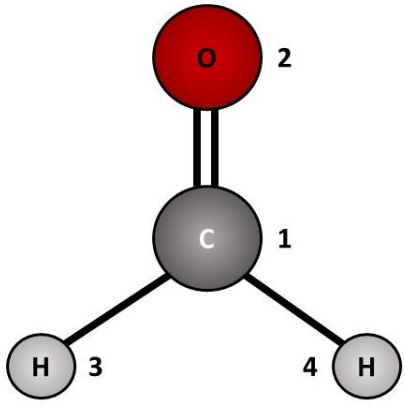

Figure 25: Geometry optimization was done prior to NMR calculations. Atom 1 is the carbon, 2 is oxygen and 3-4 are the hydrogens in the formaldehyde molecule.

As observable in Table 4, V_{ii} values along with VPPA (ΔP) and $P_{average}$ were determined and compared to the values obtained in the original paper; the values are very similar, errors stay within an average of $\pm$ 0.5 MHz for the quadrupolar coupling constant (χ_{ii}), with the biggest difference observed being 3.32 MHz for hypofluorite. The reasons for the

discrepancy are unclear, as the same protocols followed in the original paper were followed in the present work.

Table 4: Results for trial tests with ^{17}O set molecules. Reported original values from Wu[34] are italicized and given below the calculated values.

Molecule	**V_{ii} (EFG tensor components)**			**χ_{ii} (modified TD) (MHz)**			**χ_{ii} (direct calculation) (MHz)**			**ΔP_{xx}**	**ΔP_{yy}**	**ΔP_{zz}**	**P_{ave}**
				χxx	*χyy*	*χzz*	*χxx*	*χyy*	*χzz*				
Ethylene Oxide	-1.539	-0.872	2.411	-6,411 *-5.721*	-7,395 *-7.106*	13,81 *12.83*	-9.245 *-9.237*	-5.239 *-5.296*	14.48 *14.11*	-0.171 *-0.153*	-0.197 -0.190	0.367 *0.343*	1.579 *1.590*
Dimethyl ether	-1.975	-0.131	2.106	10,04 *10.00*	-11,71 *-11.66*	1,666 *1.655*	-11.87 *-11.69*	-0.788 *-0.571*	12.65 *12.26*	0.290 *0.268*	-0.319 *-0.312*	0.029 *0.044*	1.639 *1.645*
Water	-1.866	-0.102	1.967	-10,47 *-10.03*	10,57 *10.66*	-4.101 *-4.187*	-11.21 *-9.94*	-0.611 *-0.609*	11.82 *10.51*	-0.279 *-0.269*	0.281 *0.285*	-0.003 *-0.002*	1.715 *1.708*
Furan	-1,391	0,694	0,697	3,324 *3.711*	5,111 *4.712*	-8,436 *-8.422*	-8,358 *-8.338*	4,169 *3.609*	4,189 *4.729*	0,089 *0.099*	0,136 *0.126*	-0,224 *-0.226*	1,611 *1.610*
Carbon monoxide	-0.384	-0.384	0.768	-1,717 *-1.606*	-1,717 *-1.606*	3,434 *3.212*	-2.309 *-2.310*	-2.309 *-2.310*	4.617 *4.610*	-0,045 *-0.043*	-0,045 *-0.043*	0,091 *0.086*	1,573 *1.575*
Formaldehyde	-1,822	-0,322	2,144	-0,0872 *-0.343*	-10,74 *-10.43*	10,82 *10.74*	-10.95 *-10.95*	-1.934 *-1.930*	12.88 *12.88*	-0,0023 *-0.009*	-0,286 *-0.279*	0,2880 *0.288*	1,585 *1.588*
Hypofluorite	-5.698	2.849	2.849	18,29 *16.63*	18,29 *16.63*	-36,59 *-33.27*	-34.24 *-30.98*	17.12 *15.49*	17.12 *15.49*	0.487 *0.445*	0.487 *0.445*	-0.974 *-0.891*	1.513 *1.554*

The 6-311G(3df) is the basis set used and the quadrupole moment Q is -2.558 fm^2 (extracted with EFG shield program). ΔP values come from the natural bond orbital (NBO) section in the Output file, under Natural Populations: Natural atomic orbital occupancies (valence value p_x, p_y and p_z). The direct calculation *of* χ_{ii} is done using Equation 12 whereas the modified Townes Dailey calculation of χ_{ii} is done using Equation 11. Just like in the method of Wu[34], χ_0 (contribution of one single electron to the *z*-component of the QC tensor) is treated as an adjustable variable so that the plot of $1.5 * \chi_0 * \Delta P_{ii}$ in function of χ_{ii} would display a slope of unity. This method proved to be equivalent to the basis-set dependent scaling of the nuclear

quadrupole moment used in previous studies. Therefore, the value of χ_0 was modified until a value of 1 was obtained for the slope. The plot for ^{17}O molecules is shown in Figure 26 below.

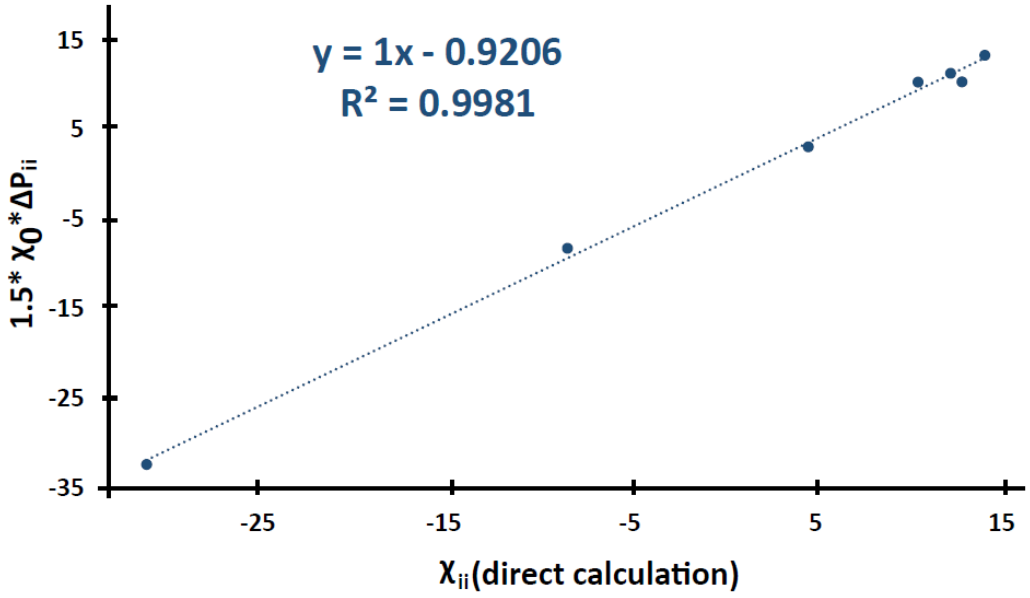

Figure 26: Plot of 1.5 *χ_0*ΔP_{ii} in function of χ_{ii} with a slope of unity to find χ_0.

χ_0 has a value of 25.05 for this example. This was compared to the 24.9 value obtained in the literature. A high R^2 value is observed (0.9981) proving a good correlation here for the ^{17}O set of molecules. The VPPA parameter has good correlation with quadrupolar coupling constant values for small molecules comprised with ^{17}O nuclei.

^{79}Br Containing Molecules

After ensuring ^{17}O results using VPPA are reproducible and consistent with reported work (Wu[34]), we move to bigger molecules and to ideally observe if VPPA can correlate well with experimental quadrupolar coupling constants. In previous group work by Szell and al.[50], ^{79}Br NQR was used to demonstrate its abilities to characterize electronic changes in the C-Br/N halogen bonding motifs found in molecules constructed from 1,4-dibromotetrafluorobenzene and nitrogen-containing heterocycles. The molecules studied with relevant information are shown in Figure 27 and Table 5. Results show that an increase in the bromine quadrupolar coupling constant is observed, which correlates linearly with the halogen bond distance.[50] In this work, the quadrupolar coupling constant C_Q and asymmetry parameter (η) were measured using a combination of pure NQR and nutation NQR. This approach demonstrated to be sensitive to small changes in the halogen bond geometry, with the C_Q in good correlation with the halogen bond length. Our motivation is to use computed VPPA data and compare with experimental ones to see the correlation and precision of the method.

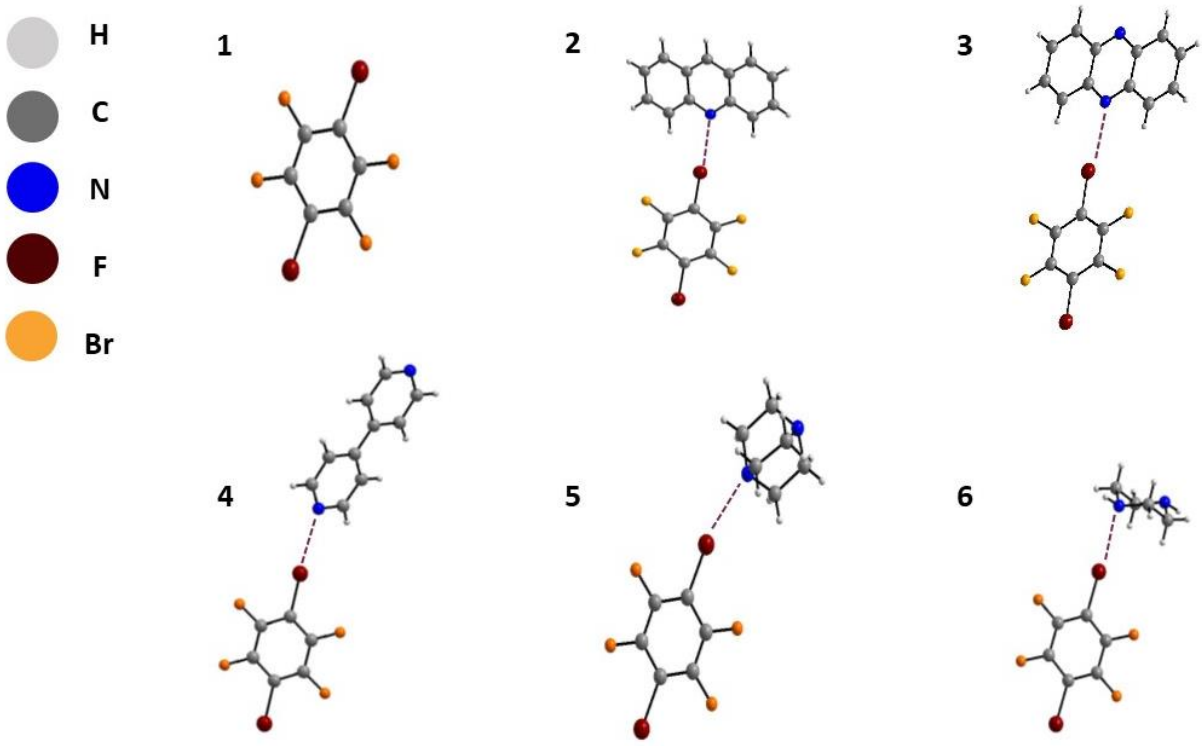

Figure 27: X-ray crystal structures of p-dibromotetrafluorobenzene (1) and its cocrystals (2–6), showing the C–Br/N halogen bond by the dashed lines. Original work from Szell et al[50]

Table 5: ^{79}Br Containing Molecules

Molecule	Compound name	Normalized distance parameter (R_{XB})[a]	Halogen bond distance (Å)	CSD reference 41
1	p-dibromotetrafluorobenzene	-	-	ZZZAVJ ref. 42
2	(acridine)(p-dibromotetrafluorobenzene)	0.891[b]	3.031[b]	712 047 ref. 43
3	(phenazine)(p-dibromotetrafluorobenzene)	0.878	2.985	712 045 ref. 43
4	(4,4'-bipyridine)(p-dibromotetrafluorobenzene)	0.846 0.876	2.878 (site A) 2.979 (site B)	199 297 ref. 44
5	(1,4-diazabicyclo[2.2.2]octane)(p-dibromotetrafluorobenzene)	0.851 0.856	2.894 (site A) 2.910 (site B)	649 676 ref. 45
6	(piperazine)(p-dibromotetrafluorobenzene)	0.847	2.881	649 675 ref. 45

[a] The normalized distance parameter R_{XB} has been calculated as the ratio between the halogen bond length ($d_{Br/N}$) and the sum of the van der Waals radii of Br and N. [b] The X-ray crystal structure shows disorder on the position of the nitrogen, resulting in two possible halogen bond geometries; the reported values herein are the averages over the two disordered halogen bond sites.

Table 6: VPPA results for ^{79}Br containing molecules. Reported experimental C_Q values from Vioglio[49] are italicized and given below calculated values.

Molecule	V_{ii} (EFG tensor components)			χ_{ii} (direct calculation) (MHz)			χ_{ii} (VPPA) (MHz)			ΔP_{xx}	ΔP_{yy}	ΔP_{zz}	P_{xx}	P_{yy}	P_{zz}	P_{ave}
				χxx	*χyy*	*χzz*	*χxx*	*χyy*	*χzz*							
1	-9.06	4.08	4.98	-666.22	299.99	366.23	-668.24 *-616.92*	357.56	310.68	-0.55	0.29	0.26	1.12	1.96	1.92	1.67
2	-9.29	4.23	5.06	-683.37	311.05	372.33	-690.87 *-634.84*	369.63	321.24	-0.57	0.30	0.26	1.09	1.96	1.92	1.66
3	-9.29	4.23	5.06	-683.37	311.05	372.33	-690.87 *-632.25*	369.63	321.24	-0.57	0.30	0.26	1.09	1.96	1.92	1.66
4a	-9.33	4.22	5.11	-686.04	310.20	375.84	-696.47 *-638.94*	373.82	322.65	-0.57	0.31	0.26	1.08	1.96	1.92	1.66
4b	-9.33	4.22	5.11	-686.04	310.20	375.84	-696.47 *-631.12*	373.82	322.65	-0.57	0.31	0.26	1.08	1.96	1.92	1.66
5a	-9.38	4.22	5.16	-689.30	310.19	379.11	-702.28 *-638.52*	375.43	326.85	-0.58	0.31	0.27	1.08	1.96	1.92	1.66
5b	-9.38	4.22	5.16	-689.31	310.20	379.11	-665.10 *-640.39*	354.36	310.74	-0.55	0.29	0.26	1.13	1.96	1.93	1.67
6	-9.37	4.22	5.15	-688.87	309.95	378.92	-685.99 *-640.57*	366.53	319.47	-0.56	0.30	0.26	1.09	1.96	1.92	1.66

The quadrupole moment Q is 31.30 fm^2 (extracted with EFG shield program) and the basis set used is DGDZVP. Comparison between the calculated χ_{ii} using VPPA and the experimental χ_{ii} from Vioglio[49] show a range of error of 24.71 to 65.35 MHz, which is 4 to 10%. Calculated χ_{ii} values are, in average, 7% higher compared to the experimental values. Just like for the ^{17}O set, in order to find χ_0, the plot of 1.5 *χ_0*ΔP_{ii} in function of χ_{ii} with a slope of unity is produced and is shown in Figure 28 below).

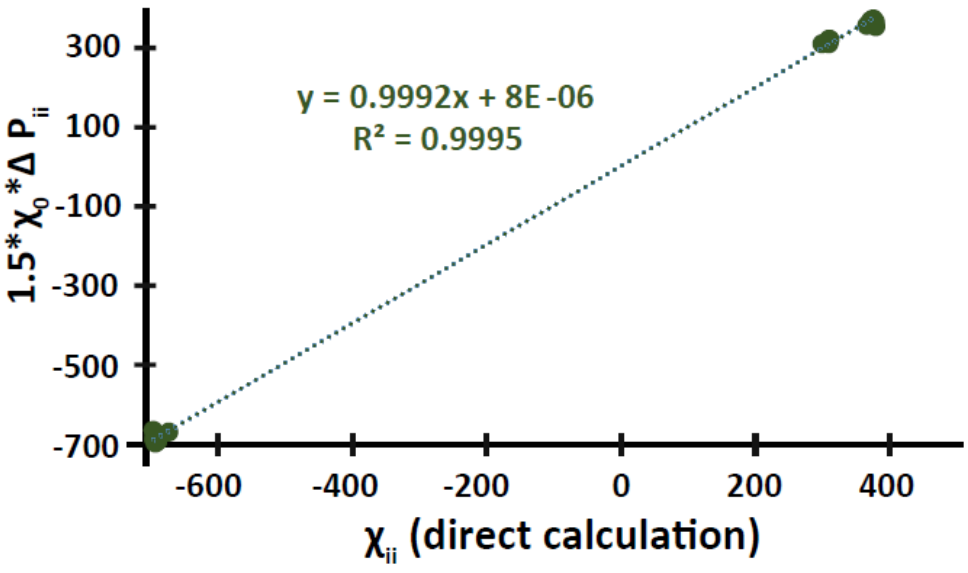

Figure 28 : Plot of 1.5 *χ_0*ΔP_{ii} in function of χ_{ii} with a slope of unity to find χ_0.

The value of χ_0 was modified until a value of 1 was obtained for the slope. χ_0 has a value of 812 MHz and since Q of Br is positive, thus to respect the convention that χ_0 must be of opposite sign to Q, χ_0 is -812 MHz. This value can be compared to the calibrated χ_0 from original work (Wu[34]) of -770 MHz. The relative error between the two is 5% and thus can be considered reasonable though not reliably precise. Some reasons explaining this difference will be discussed shortly.

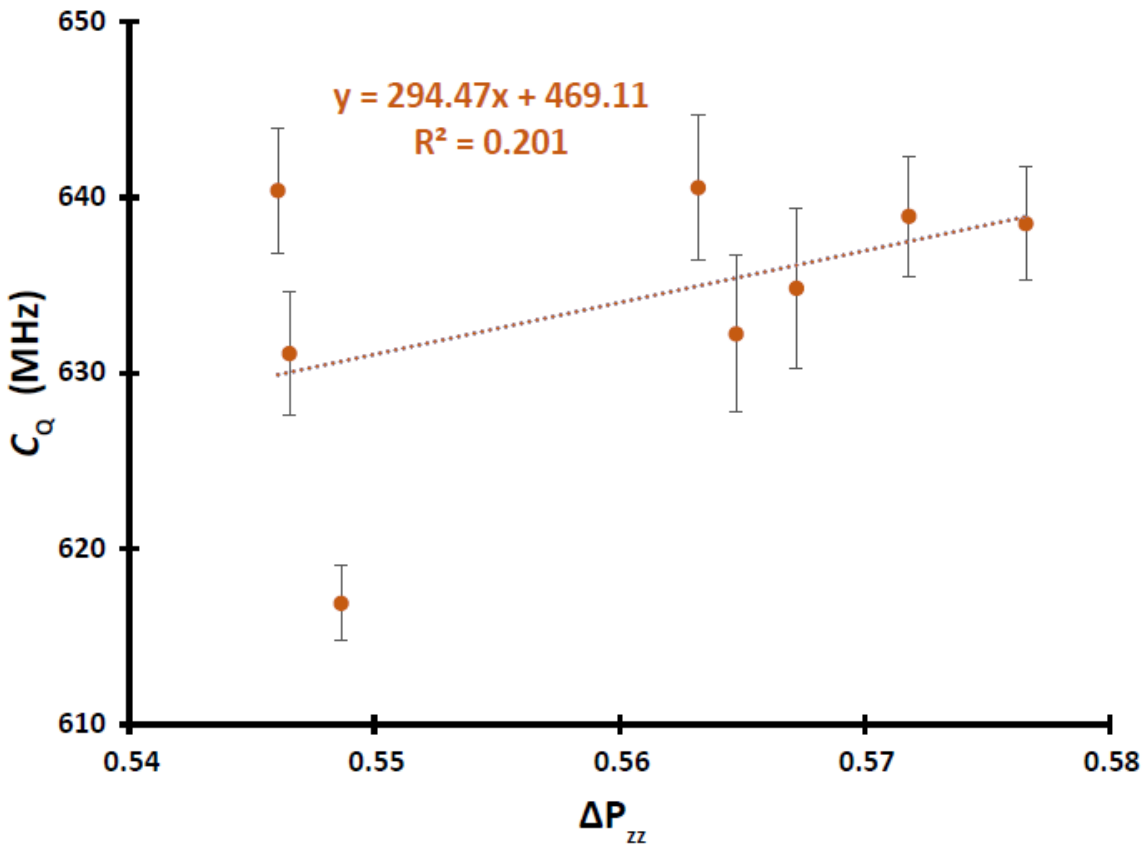

Figure 29: Plot of the experimental ^{79}Br C_Q as a function of ΔP_{zz}. Absolute values of the VPPA are plotted; the true values are negatives.

As observable in Figure 29, the correlation between ΔP_{zz} and C_Q is weak (R^2 value of 0.201). Black bars denote the experimental errors. To make the figure easier to comprehend, the absolute values of the VPPA were plotted; the true values are negative, indicative of a sigma hole.

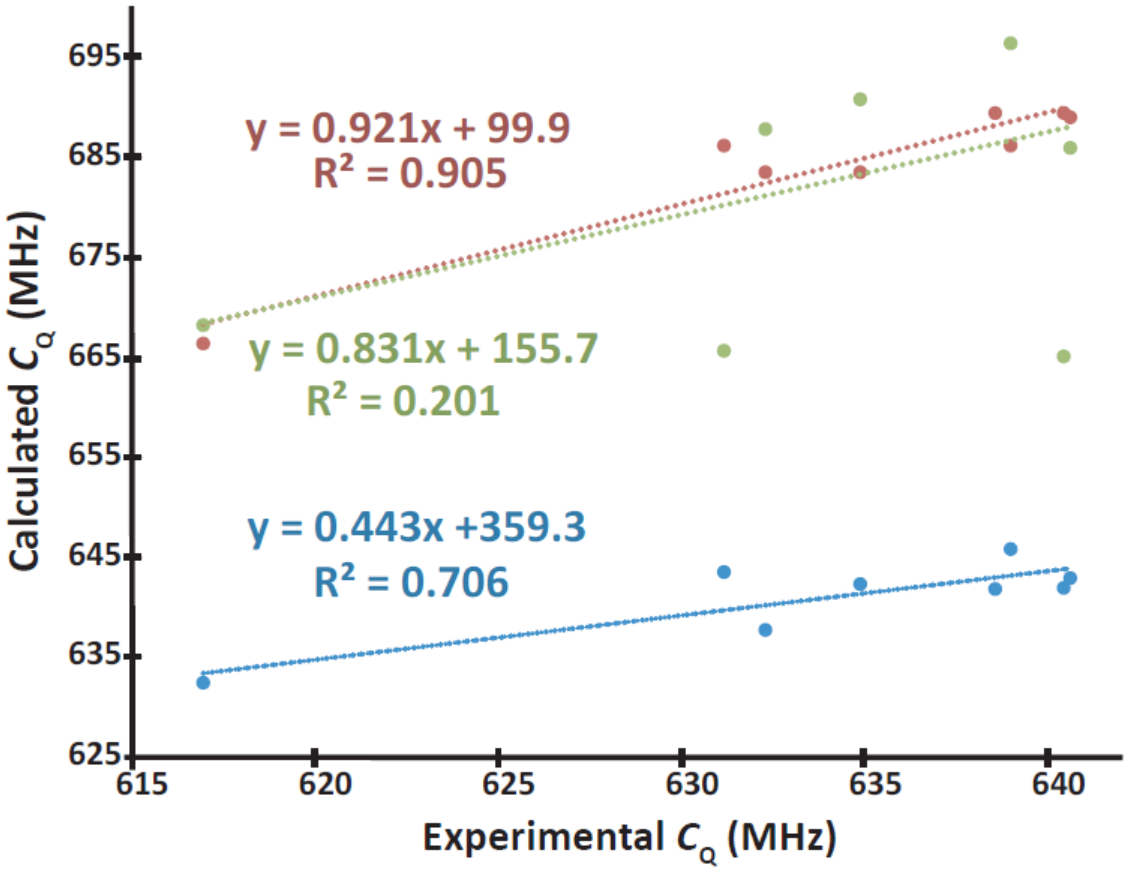

Figure 30: Plot of the DFT calculated ^{79}Br C_Q from P. Vioglio[49] (blue), reproduced DFT calculated ^{79}Br C_Q (red) and the VPPA calculated ^{79}Br C_Q (green) as a function of the experimental C_Q

Absolute values of the VPPA are plotted; the true values are negative, indicative of a sigma hole. As observable in Figure 30, R^2 values for the DFT calculated ^{79}Br C_Q from P. Vioglio[49] (blue) and the reproduced DFT calculated ^{79}Br C_Q (red) are good (respectively 0.706 and 0.905) whereas for the VPPA calculated ^{79}Br C_Q as a function of the experimental C_Q is poor (0.201). This poor correlation is explained shortly in the discussion.

^{127}I containing molecules

Once again, previous group members' published work (Szell[50]) regarding ^{127}I molecules using nuclear quadrupole resonance (NQR) is used in this last part of the project in order to observe and understand VPPA with quadrupolar coupling constants. ^{127}I NQR spectroscopy is established as a rapid and robust method to indicate the formation of iodine–nitrogen halogen bonds in co-crystalline powders. The method is demonstrated for a series of co-crystals of 1,4-diiodobenzene. Changes of up to 74.4 MHz in the ^{127}I quadrupolar coupling constant (C_Q) correlate with the length C-I donor covalent bond and inversely with the I···N halogen-bond length. We therefore observe once more if computed VPPA results correlate with the experimental quadrupolar coupling constants from Szell's[50] work. The molecules of interest are shown in Table 7 and Figure 31).

Table 7: ^{127}I containing molecules

Molecule	Compound name	Halogen bond distance (Å)	CSD reference 41
1	1,4-diiodobenzene	-	ZZZPRO08 ref. 46
1a	(1,4-diiodobenzene) (2,3,5,6-tetramethylpyrazine)	3.298	KIHQUQ ref. 47
1b	(1,4-diiodobenzene) (hexamethylene- tetramine)	2.981	QIHCIT ref. 48
1c	(1,4-diiodobenzene) (1,2-bis(4-pyridyl)ethane)	2.967	ZANQIR ref. 49
1d	(1,4-diiodobenzene) (4,4'-bipyridyl)	3.032	QIHBAK ref. 48
1e	(1,4-diiodobenzene) (4-dimethyl-aminopyridine)	3.031	DOSYUI ref. 50

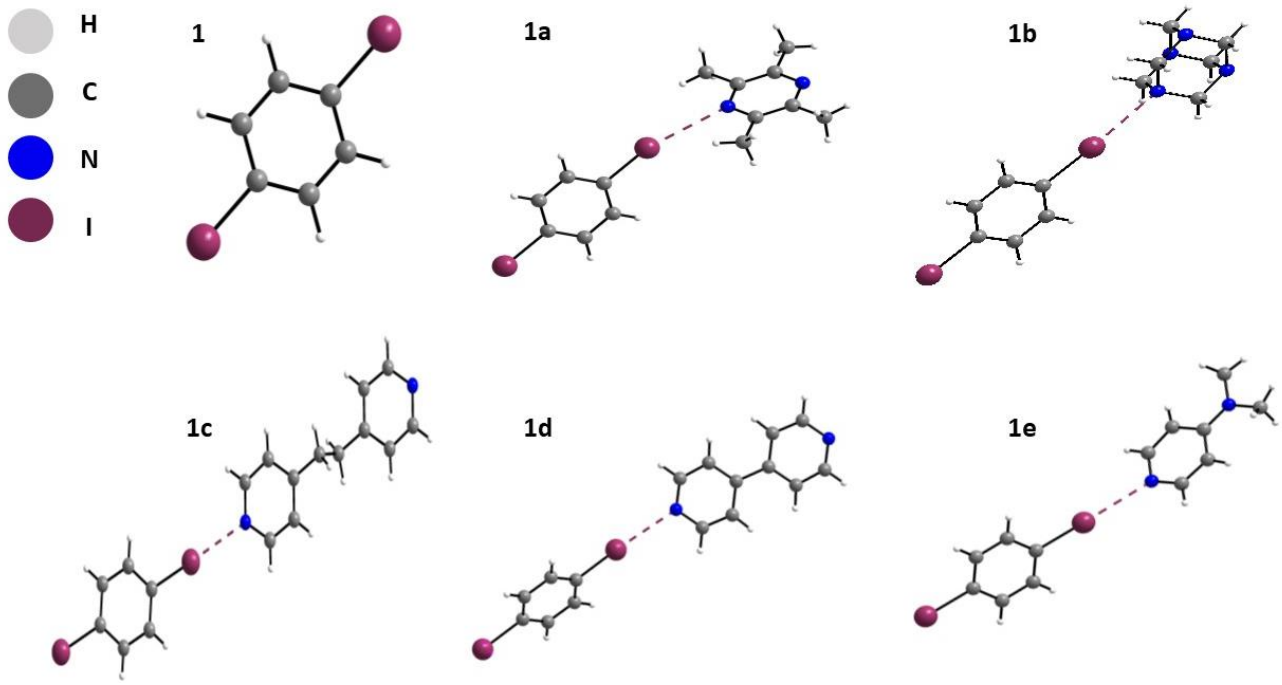

Figure 31: X-ray crystal structures of the compounds (1, 1a-1e) showing the C–I/N halogen bond by the dashed lines.

Just like for ^{17}O and ^{79}Br, the VPPA values along with V_{ii} and χ_{ii} were computed and calculated. They are shown below in Table 8.

Table 8. VPPA results for ^{127}I molecules. Reported experimental C_Q values from Szell[50] are italicized and given below my values.

Molecule	**V_{ii} (EFG tensor components)**			**χ_{ii} (direct calculation)**			**χ_{ii} (VPPA)**			**ΔP_{xx}**	**ΔP_{yy}**	**ΔP_{zz}**	**P_{xx}**	**P_{yy}**	**P_{zz}**	**P_{ave}**
				χxx	*χyy*	*χzz*	*χxx*	*χyy*	*χzz*							
1a	-11.47	5.62	5.85	1853.2	-907.94	-945.2	-1830.6 *-1893.6*	879.04	951.5	-0.616	0.2959	0.3204	1.028	1.940	1.965	1.644
1b	-11.50	5.70	5.80	1858.6	-921.20	-937.42	-1877.1 *-1915.4*	987.85	889.2	-0.632	0.3326	0.2994	1.009	1.974	1.941	1.641
1c	-11.62	5.71	5.91	1877.6	-923.06	-954.58	-1849.4 *-1901.1*	962.24	887.1	-0.623	0.3240	0.2987	1.015	1.962	1.937	1.638
1d	-11.59	5.65	5.94	1873.2	-913.69	-959.58	-1889.3 *-1911.6*	913.44	975.8	-0.636	0.3076	0.3286	1.003	1.946	1.968	1.639
1e	-11.75	5.72	6.03	1898.7	-924.42	-974.23	-1915.7 *-1914.9*	956.48	959.2	-0.645	0.3220	0.3230	0.988	1.956	1.956	1.633

The quadrupole moment Q of ^{127}I is -68.8 fm^2 (extracted with EFG shield program) and the basis set used is DGDZVP. Comparison between the calculated χ_{ii} using VPPA and the experimental χ_{ii} from Szell[50] show a range of 0.8 to 63 MHz of difference, which is 0.04 to 3%. Calculated χ_{ii} values are, in average, 7% higher compared to the experimental values. Taken in consideration the slightly different optimization and calculation run errors, which will be discussed shortly, this difference can be considered reasonable. Just like for the ^{17}O set, in order to find χ_0, the plot of $1.5 * \chi_0 * \Delta P_{ii}$ in function of χ_{ii} with a slope of unity is produced and is shown in Figure 32).

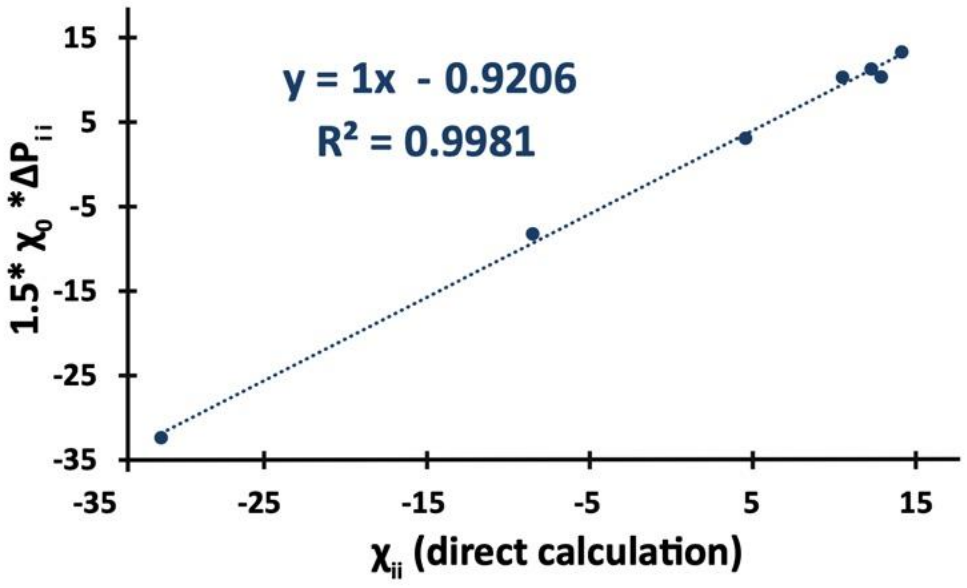

Figure 32: Plot of 1.5 *χ_0*ΔP_{ii} in function of χ_{ii} with a slope of unity to find χ_0 of ^{127}I

The value of χ_0 was modified until a value of 1 was obtained for the slope. χ_0 has a value of 1980 MHz and since Q of I is negative, thus to respect the convention that χ_0 must be of opposite sign to Q, χ_0 is 1980 MHz. This value can be compared to the calibrated χ_0 from original work (Wu[34]) of 2227 MHz. The relative error between the two is 11% and though it is higher than the relative difference for the ^{79}Br set of molecules, it is still considered similar.

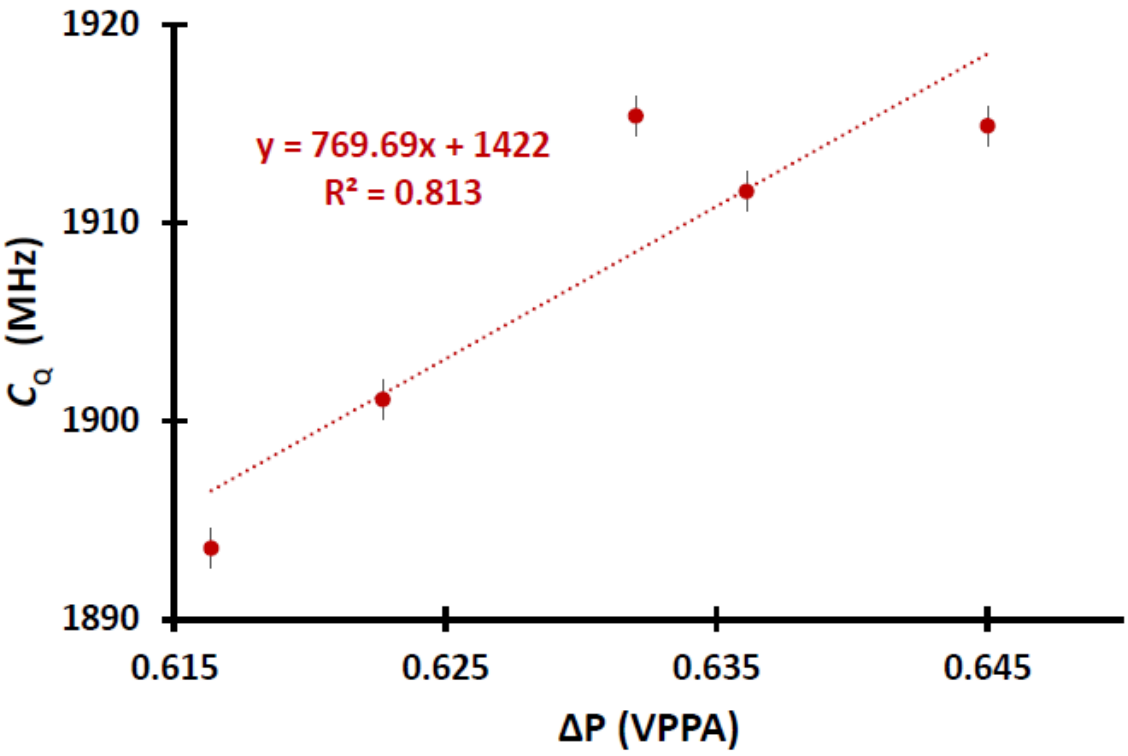

Figure 33: Plot of the experimental ^{127}I C_Q as a function of ΔP. Black bars denote the experimental errors

Absolute values of the VPPA are plotted; the true values are negative, indicative of a sigma hole. The correlation shown between the VPPA parameter and C_Q is good (R^2 value of 0.813), compared to the previous correlation for ^{79}Br (R^2 value of 0.201), both these correlations will be discussed shortly.

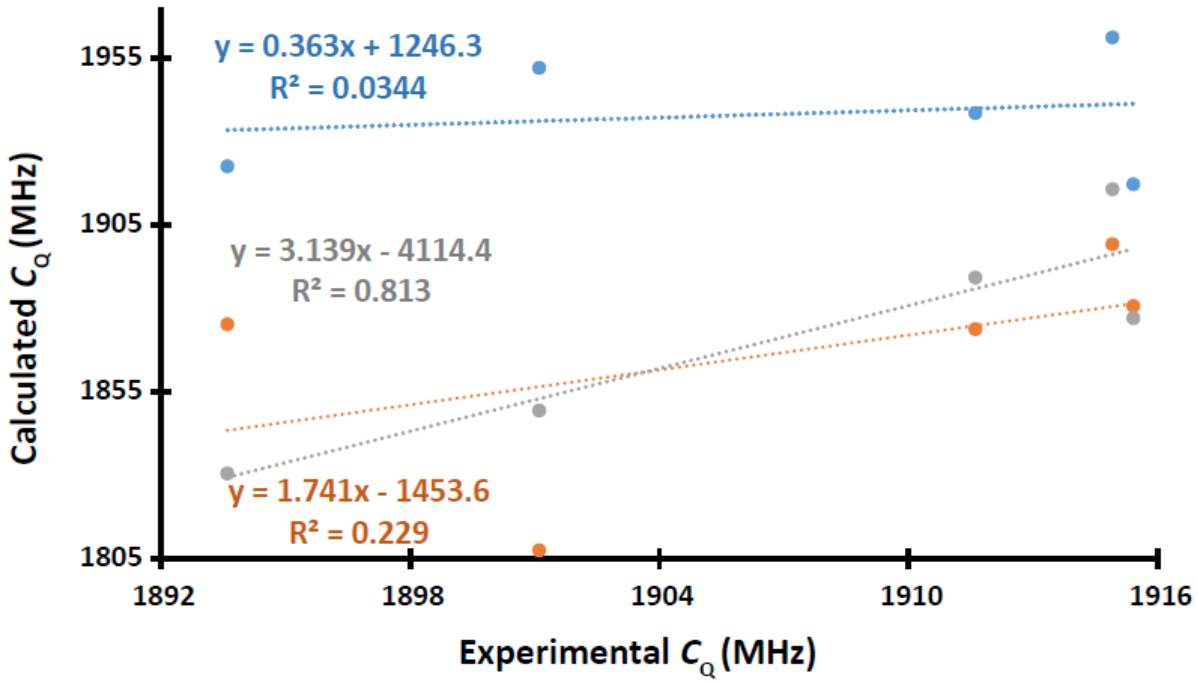

Figure 34: Plot of the DFT calculated ^{127}I C_Q from Szell[50] (blue), reproduced DFT calculated ^{127}I C_Q (orange) and the VPPA calculated ^{127}I C_Q (grey) as a function of the experimental C_Q

Absolute values of the VPPA are plotted; the true values are negative, indicative of a sigma hole. R^2 values for the DFT calculated ^{127}I C_Q from Szell[50] (blue) and the reproduced DFT calculated ^{127}I C_Q (orange) are poor (respectively 0.0344 and 0.229) whereas for the VPPA calculated ^{127}I C_Q as a function of the experimental C_Q is good (0.813).

To summarize, we tried to observe the correlation between computed quadrupolar coupling constants using VPPA and experimental data with both ^{79}Br and ^{127}I molecules. We obtain good results and correlation for iodine molecules but not bromine. Theoretically with the relativistic effect (discussed shortly), it should be observed that iodine data would have a poorer correlation than bromine if not similar. Therefore we should take into consideration some aspects of the calculation or structure optimization to explain this discrepancy. We were expecting to observe better correlation for bromine but the opposite was observed. Correlation for iodine molecules was good whereas it was poor for bromine. Some reasons explaining the poor correlation and results are:

1- Relativistic effect. This becomes more considerable with increasing atom weight (higher atomic numbers). This effect is those discrepancies between values calculated by models that consider relativity and those that do not.
2- Temperature. Computational work is done at a temperature of zero kelvin (not applicable to changes), whereas experimental work was done at room temperature. This difference in temperature might be partially responsible for discrepancies in results.
3- Choice of basis set. DGDZVP and 6-311G(3df) were the two main basis sets used in this work. The latter was great for the ^{17}O test runs as oxygen is not too big or heavy an atom. As for ^{79}Br and ^{127}I though, results done with 6-311G(3df) initially proved to be very far off from experimental values and seemed unrealistic. The DGDZVP was then chosen to its better performance and accuracy for bigger atoms. There might be other and better choices of basis sets to try for future work, but they will require more CPU time and resources to achieve.

4- Optimization of structures. Only hydrogen atom optimization was done in this work. Future work and improvement might involve optimization of the full molecule in order to achieve greater precision and accuracy.

5- VPPA just might not work as well for heavier and bigger molecules. As shown by Rinald and Wu[34], VPPA seems quite appropriate for small molecule sets and atoms lighter than bromine and iodine used in our groups' work. The VPPA parameter was not tested on larger molecules and heavier atoms, this work was a first trial in that direction.

Chapter 5 – Conclusions

The goal of the first experimental part of the masters' thesis was to observe a unique C-I···P halogen bond by means of X-ray crystallography and solid-state multinuclear magnetic resonance spectroscopy. With the mechanochemical synthesis of a novel cocrystal (dicyclohexylphenylphosphine)(1,6-diiodoperfluorohexane), one of the shortest and most linear I···P halogen bonds, with a reduced distance parameter of 0.78, was reported. The single-crystal X-ray crystal structure reveals the presence of two crystallographically distinct C-I···P halogen bonds, and solid-state NMR results support the presence of cocrystallization. A -7.0 ppm (^{31}P) chemical shift change in the cocrystal relative to pure dicyclohexylphenylphosphine is noted and proves to be consistent with halogen bond formation. Through this project, it can be established that iodoperfluoroalkanes are viable halogen bond donors when paired with phosphorus acceptors. It also shows that dicyclohexylphenylphosphine can act as a practical halogen bond acceptor.

The goal of the second project was to use a newly reported parameter, the valence p-orbital population anisotropy (VPPA), to increase the understanding of the electric field gradients' (EFGs) origins in halogen-bonded systems by computational methods. This is done and compared with previously reported extensive experimental NMR and NQR data relating ^{79}Br, ^{81}Br, and also ^{127}I quadrupolar coupling constants (C_Q) to the local molecular structure in halogen bonded systems. In order to do so, computations on model and real halogen-bonded cocrystalline systems using standard hybrid DFT methods are used to generate p-orbital populations and to compute the VPPA. Calculations and results are then compared to the experimental results from previous group work. A poor correlation is observed in the case of

^{79}Br quadrupolar coupling constants and the VPPA parameter for systems featuring bromine halogen bonds (R^2 value of 0.201) whereas good correlation is seen between experimental ^{127}I quadrupolar coupling constants and the VPPA parameter for systems featuring iodine halogen bonds (R^2 value of 0.813). Iodine data show that the experimental ^{127}I quadrupolar coupling constants directly reflect *p*-orbital population anisotropy in halogen-bonded systems.

As for future steps, further work with the bromine sets can help determine if the poor agreement is real or due to artefacts in the approach taken. Other (larger) basis sets (which weren't possible in this project du to time and resources constraints) may be used to compare the results obtained.

Overall, the work reported in this thesis has contributed to an increased experimental and computational understanding of halogen bonded systems and their NMR parameters.

References

[1] Martin E., Hine R. A Dictionary of Biology (6 ed.). Oxford University Press. **2008**. DOI: 10.1093/acref/9780199204625.001.0001.

[2] Rye C., Wise R., Jurukovski V., DeSaix J., Choi J., Avissar Y. R. RICE University. Houston, Texas. **2018**. https://openstax.org/details/books/biology-2e

[3] Petrucci, Ralph H., et al. General Chemistry: Principles and Modern Applications. Upper Saddle River, NJ: Prentice Hall, **2007**

[4] Dumas J. M., Gomel M., Guerin M. John Wiley & Sons Ltd, New York, **1983**, pp 985–1020.

[5] Dumas J.M., Peurichard H., Gomel M. *J. Chem. Res.* **1978,** 2: 54–57.

[6] Gilday L. C., Robinson S. W., Barendt T. A., Langton M. J., Mullaney B. R., Beer P. D. *Chem. Rev.* **2015**, 115: 7118–7195.

[7] Desiraju G. R., Ho P. S., Kloo L., Legon A.C., Marquardt R., Metrangolo P., Politzer P., Resnati G., Rissanen K. *Pure Appl. Chem.* **2013**, 85: 1711–1713.

[8] Clark T., Hennemann M., Murray J, Politzer P. *J. Mol. Model.* **2007**, 13: 291-296.

[9] Metrangolo P., Neukirch H., Pilati T., Resnati G. *Acc. Chem. Res.* **2005**, 38, 5: 386-395 .

[10] Corradi E., Meille S.V., Messina M.T., Metrangolo P., Resnati G.. *Angew. Chem., Int. Ed.* **2000**, 39: 1782-1786.

[11] Brammer, L. *Faraday Discuss.* **2017**, 203: 485–507.

[12] Weingarth M., Raouafi N., Jouvelet B., Duma L., Bodenhausen G., Boujlel K., Schollhorn B., Tekely P. *Chem. Commun.* **2008**, 5981–5983.

[13] Silverstein R.M., Webster F.X., Kiemle D.J., Bryce D.L. "Identification spectrométrique de composés organiques", 3rd ed. De Boeck, **2016**.

[14] Brian Zinkel. IR vs NMR Spectroscopy: What's the difference? Benchtop NMR Blog. Nanalysis. Jan 21, 2019. https://www.nanalysis.com/nmready-blog/2019/1/21/ir-vs-nmr-spectroscopy-whats-the-difference

[15] William Reusch. Nuclear Magnetic Resonance Spectroscopy. Michigan State University. May 5, 2013. https://www2.chemistry.msu.edu/faculty/reusch/virttxtjml/spectrpy/nmr/nmr1.htm

[16] Michigan State University. College of Natural Science. Max T. Rogers NMR 900 MHz Facility. NMR applications. https://nmr.natsci.msu.edu/experiments/nmr-applications/

[17] Levitt M. H. Spin dynamics: basics of nuclear magnetic resonance. 2nd ed. John Wiley & Sons, New York, **2001**

[18] Man P.P. Encyclopedia of Analytical Chemistry: applications, theory and instrumentation. R.A. Meyers Ed, John Wiley & Sons, New York, **2000**

[19] Gerstein B.C. Nuclear Magnetic Resonance (NMR). In: Meyers R.A., editor. Encyclopedia of Physical Science and Technology—Analytical Chemistry. 3rd ed. San Diego, **2001**

[20] Odelius M., Laaksonen A. *J Theor Comput Chem.* **1999**, 7: 299-308.

[21] Kaseman D.C., McKenny M. Quadrupolar Coupling. Chemistry Libretexts. Aug 15, 2020. https://chem.libretexts.org/Bookshelves/Physical_and_Theoretical_Chemistry_Textbook_Maps/Supplemental_Modules_(Physical_and_Theoretical_Chemistry)/Spectroscopy/Magnetic_Resonance_Spectroscopies/Nuclear_Magnetic_Resonance/NMR_-_Theory/NMR_Interactions/Quadrupolar_Coupling

[22] Trontelj Z., Pirnat J., Jazbinsek V., Luznik J., Srcic S., Lavric Z., Begus S., Apih T., Zagar V., Seliger J. *Crystals.* **2020**, 10: 450-472.

[23] Poleshchuk O.K., Latosinska J.N. *Nucl. Quad. Res. Appl.* **1999**. 2: 1653-1662.

[24] Suits B.H. Nuclear Quadrupolar Resonance Spectroscopy, In: Vij, D. (eds) Handbook of Applied Solid State Spectroscopy. Springer, Boston. **2006**

[25] Poleshchuk O.K., Latosinska J.N. *Nucl. Quad. Res. Appl.* **1999**. 2: 1653-1662.

[26] Finocchi F. Density Functional Theory for Beginners: Basic principles and practical approaches. Institut des NanoSciences de Paris (INSP) CNRS and University Pierre et Marie Curie. October 2011.

[27] Jakubikova E. DFT for (almost) Beginners. Chemistry Department, North Carolina State University. http://hybrid3.duke.edu/sites/hybrid3.duke.edu/files/u63/dft_HybriD3_jakubikova.pdf

[28] Burke K., Wagner L. Basics of DFT. Departments of Physics and of Chemistry, University of California, October 2012.

[29] Gordon M.H. *J. Phys. Chem.* **1996**, 100: 13213-13225

[30] Tomberg A., Gaussian 09W Tutorial, An introduction to computational chemistry using g09w and avogadro software

[31] Riley K.E., Tran K-A., Lane P., Murray J.S., Politzer P. *J Comp Sci.,* **2016,** 17: 273–284.

[32] Siiskonen A, Priimagi A., *J Mol Model.,* **2017,** 23: 50-59

[33] Glendening E., Landis C., Weinhold F. What are NBOs (and Other "Natural"-type Orbitals)? Last updated on February 8th 2021 https://nbo7.chem.wisc.edu/webnbo_css.htm

[34] Rinald A., Wu Gang. *J. Phys. Chem A.* **2020**, 124: 1176-86.

[35] Novick S. *J. Mol Spectrosc.* **2011**, 267: 13-18.

[36] Xu Y., Szell P. M. J., Kumar V., Bryce D. L. *Coord. Chem. Rev*., **2020,** 411: 213-237.

[37] Frisch M.J., Trucks G.W., Schlegel et al. Gaussian 09 Revision D.01, Gaussian Inc., Wallingford, CT, 2013.

[38] The Woo Lab, University of Ottawa. 2022. http://titan.chem.uottawa.ca/

[39] Dennington R., Keith T., Milliam J. *GaussView Version 4.1*. Semichem Inc. Shawnee Mission, KS 2007.

[40] Adiga S., Aebi D., Bryce D. L. *Can. J. Chem.*, **2007**, 85: 1036-1046.

[41] Groom C. R., Bruno I. J., Lightfoot M. P., Ward S. C. *Acta Crystallogr., Struct. Sci., Cryst. Eng. Mater.,* **2016**, 72: 171–179.

[42] Pawley G. S., Mackenzie G. A., Dietrich O. W., *Acta Crystallogr., Cryst. Phys., Diffr., Theor. Gen. Crystallogr.,* **1977**, A33: 142–145.

[43] Cinčić D., Friščić T., Jones W. *Chem. Mater.,* **2008**, 20: 6623–6626.

[44] Santis A., Forni A., Liantonio R., Metrangolo P., Pilati T., Resnati G. *Chem. Eur. J.,* **2003**, 9: 3974–3983.

[45] Cinčić D., Friščić T., Jones W. *Chem. Eur. J.,* **2008**, 14: 747–753.

[46] Popp S., Bolte M. *CSD Communication,* **2011.** https://doi.org/10.5517/ccw94pz

[47] Szell P.M.J., Gabriel S., Caron-Poulin E., Jeannin O., Fourmigué M., Bryce D. *Cryst. Growth Des*. **2018**, 18: 6227 – 6238.

[48] Walsh R. B., Padgett C. W., Metrangolo P., Resnati G., Hanks T. W., Pennington W. T. *Cryst. Growth Des.* **2001**, 1: 165-175.

[49] Vioglio P.C, Catalano L., Vasylyeva V., Nervi C., Chierotti M.R, Resnati G., Gobetto R., Metrangolo P. *Chem. Eur. J.*, **2016**, 22: 16819-16828.

[50] Szell P. M. J., Grébert L., Bryce D.L, *Angew. Chem. Int. Ed.* **2019**, 58: 13479-13485.